

# Regional and teleseismic analysis of underground nuclear explosion waveforms and constraints for shear wave excitation mechanisms

Tae-Kyung Hong<sup>1</sup>

Received 8 February 2009; revised 23 December 2009; accepted 4 January 2010; published 11 June 2010.

[1] Regional and teleseismic waveforms of underground nuclear explosions (UNEs) at the Balapan and the Nevada test sites are analyzed to understand the nature of shear waves excited from UNEs. The phase composition of wavefields in the source and receiver regions is examined using a source array frequency-wave-number analysis and polarization analyses. It is observed that regional mantle-lid shear waves,  $S_n$ , often develop strongly. On the other hand, observed teleseismic shear waves from UNEs are much weaker than those from earthquakes. Source array analyses of the shear waves from UNEs display coherent energy that is polarized in a certain azimuthal direction. The observation of coherent shear energy in different UNEs suggests that the shear energy is excited in a consistent manner at every UNE. We constrain the dominant shear wave excitation mechanism from the observed shear wave features. The observations appear to be consistent with the tectonic release model with conical rock cracking.

**Citation:** Hong, T.-K. (2010), Regional and teleseismic analysis of underground nuclear explosion waveforms and constraints for shear wave excitation mechanisms, *J. Geophys. Res.*, 115, B06306, doi:10.1029/2009JB006368.

## 1. Introduction

[2] Understanding the mechanism of shear wave excitation from underground nuclear explosions (UNEs) is a key issue for successful discrimination of UNEs from natural earthquakes. Various mechanisms have been proposed to explain the excitation of shear waves from UNEs. The proposed mechanisms include  $Rg$ -to- $S$  scattering [e.g., Gupta *et al.*, 1992; Myers *et al.*, 1999],  $S^*$  [e.g., Gutowski *et al.*, 1984; Vogfjörd, 1997], tectonic release [e.g., Toksöz and Kehrner, 1972; Ekström and Richards, 1994], rock cracking [e.g., Massé, 1981], and spall [e.g., Stump, 1985; Day and McLaughlin, 1991]. However, the community has not reached consensus on the major shear wave excitation mechanisms yet.

[3] The dominant shear wave excitation mechanisms may be possibly resolved from phase composition and shear wave radiation patterns in the source region. Recent advances in source array analysis of regional and teleseismic records allow us to examine the phase composition of wavefields in the source region [Hong and Xie, 2005; Hong and Menke, 2008]. Because the source array analysis is based on the seismic records of events that occurred at different origin times, it naturally suppresses the influence of seismic noise that varies with time. Thus, the source array analysis enables us to resolve the time-invariant features

of phases. It was recently reported that  $S$  phases are uniquely excited from the source region [Hong and Xie, 2005; Hong and Menke, 2008].

[4] Comparison of shear-energy composition between regional and teleseismic wavefields is important for understanding the dependency of shear-energy excitation on the take-off angle. Regional phases are generated by energy radiated from the source at large take-off angles. These waves naturally travel through the crust and/or the mantle lid. On the other hand, teleseismic waves evolve from the energy radiated near vertically from the source and travel mostly through the mantle and the core. Investigation of regional and teleseismic phase compositions will then allow us to infer the nature of the sources responsible for shear wave excitation. In this study, we analyze regional and teleseismic records for UNEs in the Balapan and Nevada test sites.

## 2. Data

[5] Seismic records for the Balapan UNEs during 1975–1985 and the Nevada UNEs during 1988–1992 are collected. Ground-truth or high-precision information for event locations and origin times are available from various sources [Adushkin *et al.*, 1997; Kim *et al.*, 2001; Thurber *et al.*, 2001; Trabant *et al.*, 2002; Springer *et al.*, 2002]. The source parameters of the Balapan and Nevada UNEs analyzed in this study are presented in Tables 1 and 2.

[6] The magnitudes ( $m_b$ ) of the Balapan UNEs range between 5.4 and 6.1, while those of the Nevada UNEs are between 5.3 and 5.9. The depths of the Balapan UNEs are 359–708 m, and those of the Nevada UNEs are 542–674 m.

<sup>1</sup>Department of Earth System Sciences, Yonsei University, Seoul, South Korea.

**Table 1.** Source Parameters of the Balapan UNEs Analyzed in This Study<sup>a</sup>

Date	Time	Lat. (°)	Long. (°)	Dep. (m)	$m_b$	Station (time shift in s)
12/27/1974	05:46:59.35	49.965	79.003	416	5.5	K(-3.68)
10/29/1975	04:46:59.82	49.953	78.873	433	5.6	K(-7.67)
12/25/1975	05:16:59.65	50.043	78.820	435	5.6	K(-5.67)
07/04/1976	02:56:59.94	49.904	78.899	444	5.8	K(-9.38)
08/28/1976	02:56:59.99	49.975	78.926	448	5.7	K(-8.37)
11/23/1976	05:02:59.75	50.013	78.943	453	5.7	K(-9.31)
12/07/1976	04:56:59.85	49.943	78.839	454	5.8	K(-5.80)
05/29/1977	02:57:00.01	49.946	78.771	460	5.7	K(2.42)
09/05/1977	03:02:59.86	50.055	78.914	468	5.7	K(12.51)
06/11/1978	02:57:00.08	49.913	78.801	487	5.8	K(-52.74)
08/29/1978	02:37:08.75	50.006	78.967	494	5.9	K(3.36)
09/15/1978	02:36:59.90	49.928	78.861	496	5.8	K(2.42)
06/23/1979	02:57:00.02	49.914	78.845	521	6.1	K(-3.39)
07/07/1979	03:46:59.81	50.033	78.989	522	5.8	K(5.38)
08/04/1979	03:56:59.97	49.903	78.887	526	6.1	K(10.86)
08/18/1979	02:51:59.61	49.948	78.918	528	6.1	K(9.02)
10/28/1979	03:16:59.45	49.996	78.995	538	5.9	K(13.93)
06/29/1980	02:33:00.19	49.948	78.818	552	5.6	K(3.21)
10/12/1980	03:34:16.58	49.967	79.022	558	5.8	K(10.34)
03/29/1981	04:03:52.51	50.018	78.978	568	5.4	K(-3.08)
09/13/1981	02:17:20.76	49.913	78.894	577	6.0	K(-0.88)
10/18/1981	03:57:05.14	49.928	78.844	582	6.0	K(-4.99)
12/27/1981	03:43:16.62	49.933	78.778	587	6.1	K(-1.75)
12/05/1982	03:37:15.04	49.930	78.809	604	6.0	K(0.91)
12/26/1982	03:35:16.68	50.063	78.993	606	5.5	K(-2.45)
02/19/1984	03:57:05.85	49.896	78.743	632	5.7	K(-5.77)
03/29/1984	05:19:10.66	49.911	78.926	634	5.8	K(-0.73)
04/25/1984	01:09:05.99	49.935	78.850	636	5.9	K(0.38)
12/16/1984	03:55:05.07	49.945	78.808	657	6.1	K(-0.92)
02/10/1985	03:27:09.98	49.899	78.780	659	5.8	K(0.94)
04/03/1987	01:17:10.28	49.918	78.780	671	6.1	C(-0.05)
06/20/1987	00:53:07.09	49.935	78.744	518	6.0	C(-0.04), W(-0.02)
08/02/1987	00:58:09.27	49.880	78.874	683	5.8	C(0.11)
11/15/1987	03:31:09.08	49.898	78.758	499	5.9	W(-0.11)
12/13/1987	03:21:07.31	49.963	78.793	530	6.0	C(0.08), H(0.04), T(0.26), W(0.17)
12/27/1987	03:05:07.00	49.879	78.725	530	6.0	C(-0.12), T(0.16), W(-0.26)
02/13/1988	03:05:08.32	49.936	78.863	526	5.9	H(0.09), T(0.25), W(0.12)
04/03/1988	01:33:08.29	49.908	78.908	502	5.9	C(0.13), H(-0.01), T(0.43), W(-0.06)
05/04/1988	00:57:09.26	49.949	78.750	519	6.0	T(-0.27), W(0.09)
09/14/1988	03:59:59.69	49.877	78.823	518	6.0	C(0.14), H(-0.12), M(-0.12), T(-0.19), W(-0.16)
12/17/1988	04:18:09.29	49.881	78.924	642	5.8	M(0.08), L(0.01), T(-0.09), W(0.03)
01/22/1989	03:57:09.02	49.939	78.819	708	6.1	C(-0.09), H(-0.08), M(-0.07), L(-0.08), T(-0.27)
02/12/1989	04:15:09.34	49.918	78.711	572	5.8	C(-0.06), H(0.10), M(0.11), L(0.10), T(-0.08), W(0.20)
07/08/1989	03:47:00.03	49.867	78.780	359	5.5	C(0.03), H(-0.04), L(0.07), W(0.07)
10/19/1989	09:49:59.81	49.922	78.908	455	5.8	C(-0.16), H(0.03), M(-0.00), L(-0.09), T(-0.20), W(-0.06)

<sup>a</sup>The depth values are collected from *Hong and Xie* [2005], who calculate the depths from a relationship between magnitudes and depths. Seismic records are collected from seven GSN stations: COL (C), HIA (H), KHC (K), KMI (M), LZH (L), TOL (T), WMQ (W). The names of stations used are presented for each event. The time shifts made in the waveform alignment are annotated at every station.

The events were recorded by regional and teleseismic stations of the Global Seismographic Network (GSN) (Figures 1 and 2). We choose spatially clustered UNEs for a source array analysis. The seismic data are corrected for the instrument responses before analyses.

[7] The Balapan test site is placed on the Precambrian and Paleocene hard-rock basement [*Levashova et al.*, 2003]. The Nevada test site is placed on volcanic rock regions with host rocks of either rhyolite or tuff [*Springer et al.*, 2002].

### 3. Methods

#### 3.1. Source Array Slowness-Wave-Number Analysis

[8] We examine the phase composition in the source region using a source array analysis. A source array is based

on single-station waveforms for spatially clustered events occurring at different origin times. The source array records are often misaligned due to the errors in event locations, origin times, or recording times. The misalignment of source array records can be corrected by aligning a certain phase with respect to a reference travel-time curve based on a global Earth model. We use the 1-D reference Earth model ak135 of *Kennett et al.* [1995] for calculation of the reference travel-time curve. The phase alignment is done using a cross-correlation technique [*Hong and Xie*, 2005].

[9] We perform a frequency-wave number (F-K) analysis to identify the phase velocities and the propagation directions of coherent waves observed over the array. A source array F-K analysis resolves the phase composition in the

**Table 2.** Source Parameters of the Nevada UNEs<sup>a</sup>

Date	Time	Lat. (°)	Long. (°)	Dep. (m)	$m_b$	Station (time shift in s)
02/15/1988	18:10:00.09	37.314	-116.472	542	5.4	C(-0.05), F(-0.14)
06/02/1988	13:00:00.09	37.260	-116.442	620	5.5	C(0.06), F(-0.03), P(-0.33)
07/07/1988	15:05:30.07	37.252	-116.378	622	5.9	P(-0.46)
08/17/1988	17:00:00.09	37.297	-116.307	616	5.6	C(0.03)
06/22/1989	21:15:00.08	37.283	-116.413	544	5.4	C(0.02), P(0.14)
06/27/1989	15:30:00.02	37.275	-116.354	640	5.3	P(0.16)
10/31/1989	15:30:00.09	37.263	-116.492	564	5.8	A(-0.10), C(-0.10), F(-0.04), R(-0.07)
12/08/1989	15:00:00.09	37.231	-116.410	601	5.7	A(-0.06), C(-0.00), F(0.31), P(0.16), R(0.05)
06/13/1990	16:00:00.09	37.262	-116.421	674	5.8	A(-0.03), C(-0.00), F(-0.05), R(-0.00)
10/12/1990	17:30:00.08	37.248	-116.495	600	5.8	A(-0.07), C(-0.13), F(-0.06), R(-0.04)
11/14/1990	19:17:00.07	37.227	-116.372	594	5.7	C(0.03)
04/04/1991	19:00:00.00	37.296	-116.314	629	5.6	C(0.05)
04/16/1991	15:30:00.07	37.245	-116.443	642	5.6	A(0.19), C(0.11), P(0.17), R(0.02)
09/14/1991	19:00:00.08	37.226	-116.429	658	5.8	A(-0.10), C(-0.03), F(0.03), P(0.13), R(-0.05)
03/26/1992	16:30:00.00	37.272	-116.361	622	5.6	A(0.18), C(-29.98), P(0.01), R(0.10)

<sup>a</sup>Seismic records are collected from five GSN stations: ANMO (A), COR (R), COL (C), PAS (P), and PFO (F). The names of stations along with the time shifts are displayed for every event.

source region. The F-K analysis is based on a stacked slowness power spectrum,  $P_W$ , which is given by [Hong and Xie, 2005]

$$P_W(\mathbf{s}) = \frac{1}{N} \sum_{j=1}^N |U(\omega_j \mathbf{s}, \omega_j)|^2 / m_j, \quad (1)$$

where  $\omega_j$  ( $j = 1, 2, \dots, N$ ) is a discrete frequency,  $N$  is the number of discrete angular frequencies,  $\mathbf{s}$  is the slowness vector, and  $U$  is a discrete double-Fourier spectrum of array waveforms. The parameter  $m_j$  is a normalization (whitening) factor that corrects for seismic attenuation [Hong and Xie, 2005].

[10] The array analysis yields valid results when the array aperture is sufficiently small with respect to the curvatures of incoming wavefronts. Also, the array should be composed of a sufficient number of array components to increase the

resolution. Spatially clustered nuclear explosions are useful for a source array analysis. The vertical locations of the source arrays are determined by the source depths. The average depth of the Balapan UNEs is 538 m with a standard deviation of 79 m. The average depth of the Nevada UNEs is 611 m with a standard deviation of 37 m. Considering the horizontal apertures of source arrays and the wavelengths of seismic phases, vertical variations of source array components are negligible. Thus, the source arrays can be assumed to be placed on common horizontal planes [Hong and Xie, 2005]. The high-precision information of event locations enables us to accurately resolve the phase composition of coherent waves in the array records.

### 3.2. Polarization Analysis

[11] The presence of shear energy in waveform records can be examined using polarization analyses that estimate

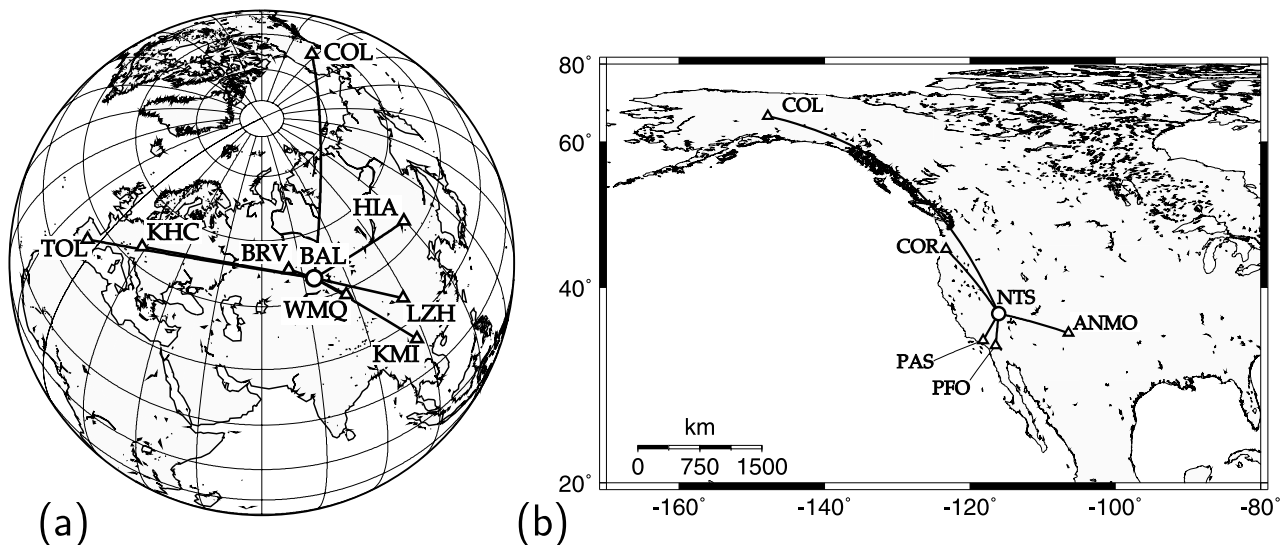


**Figure 1.** Location maps of underground nuclear explosion (UNE) test sites and stations: (a) the Balapan test site and (b) the Nevada test site. The great circle paths between the UNEs and stations are presented with solid lines. The UNEs are spatially clustered.

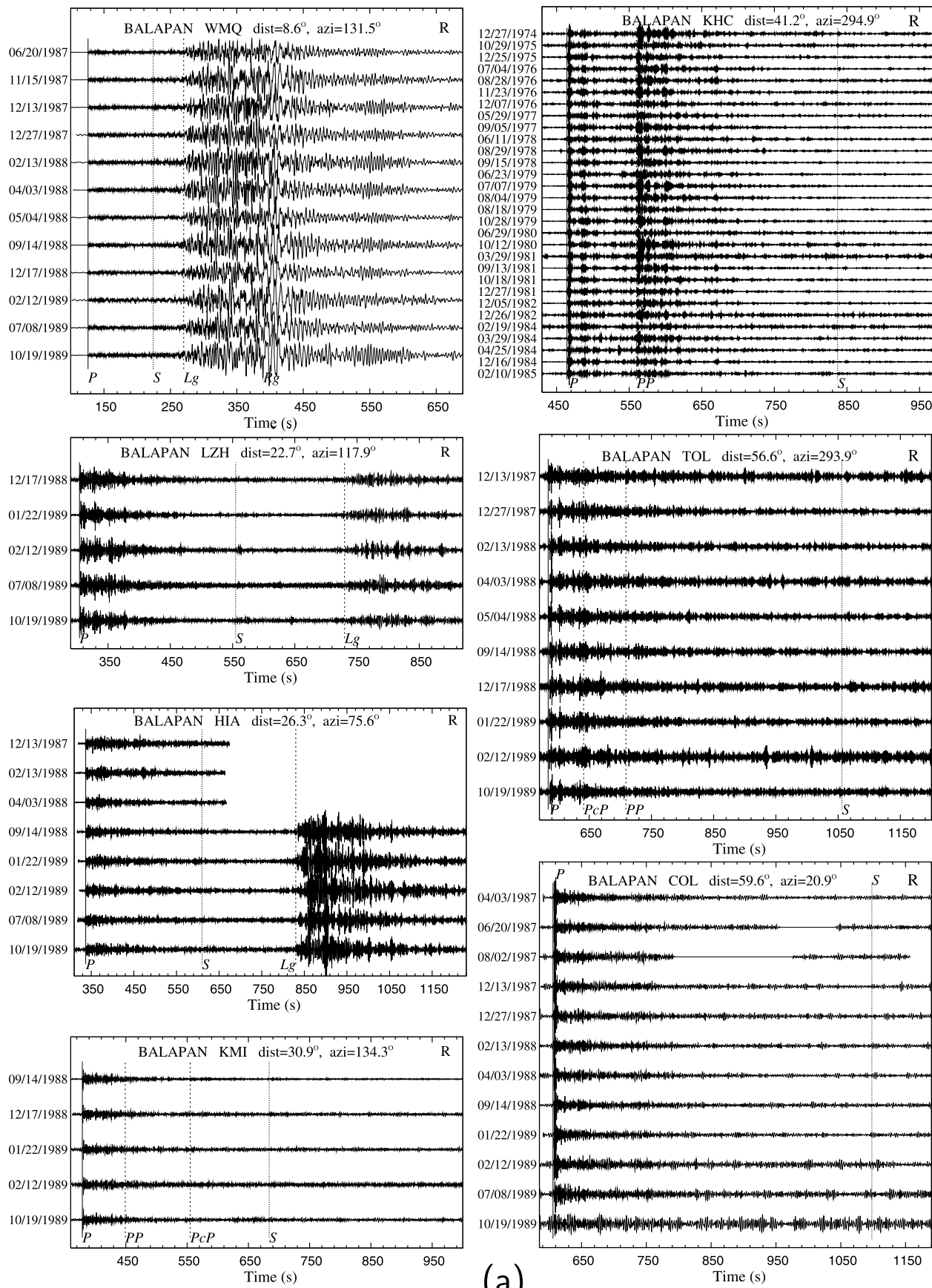


Figure 2

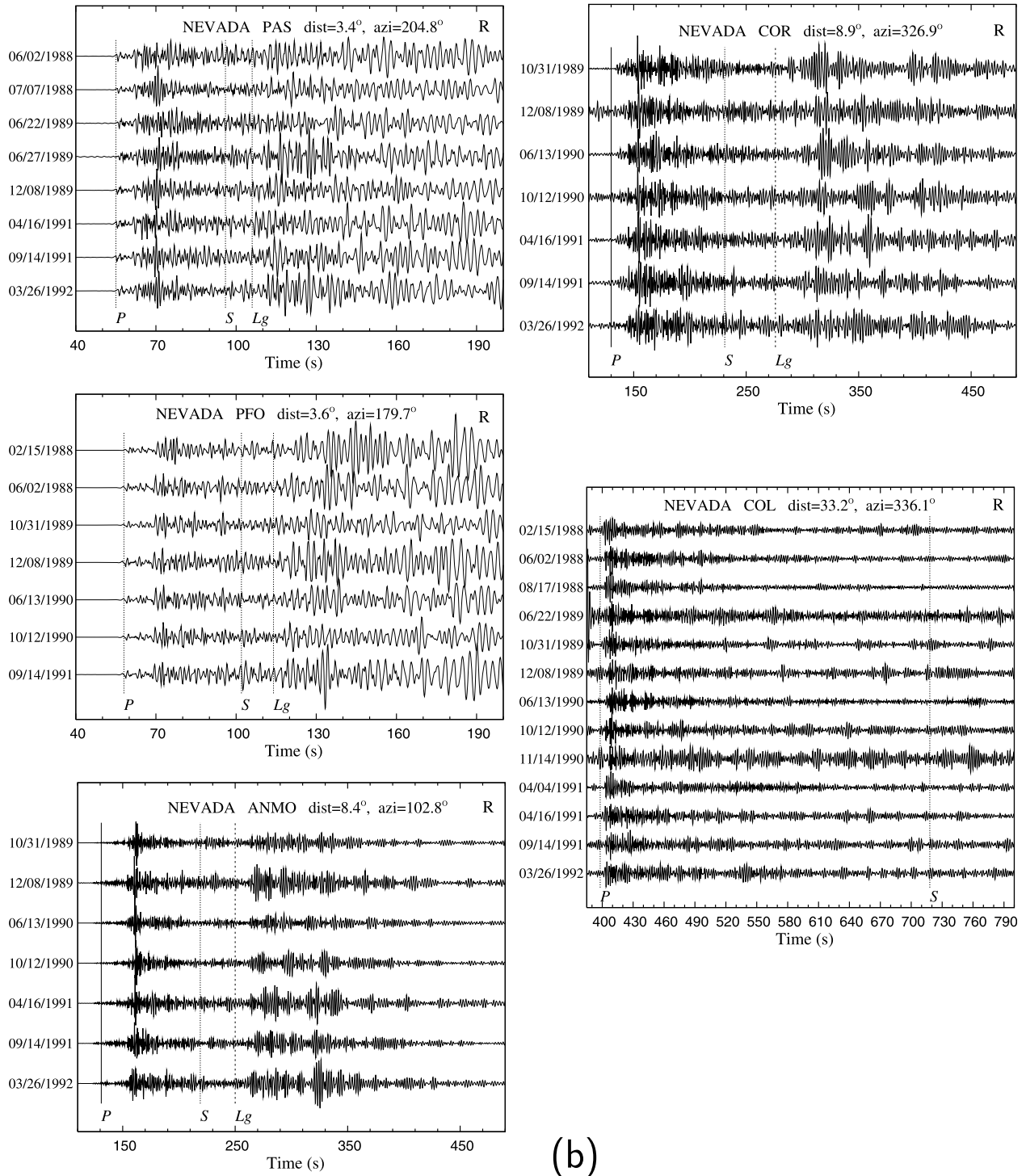


Figure 2. (continued)

Figure 2. Seismic waveforms on radial components for (a) the Balapan UNEs and (b) the Nevada UNEs. A bandpass filter between 0.5 and 2.5 Hz is applied. The record sections are normalized for a common level. The event dates are denoted on the left margins of the record sections. Station names, distances and azimuths are displayed on record sections. Theoretical arrival times of major seismic phases are marked with dotted lines.

the direction of polarization, rectilinearity, and planarity of wave. The horizontal polarization direction of a wave,  $\psi_h$ , is determined by [Vidale, 1986; Jurkevics, 1988]

$$\psi_h = \tan^{-1} \left[ \frac{u_{e1} \text{sign}(u_{z1})}{u_{n1} \text{sign}(u_{z1})} \right], \quad (2)$$

where  $u_{i1}$  ( $i = z, n, e$ ) is the direction cosine of the eigenvector with the largest eigenvalue for the covariance matrix. The parameter  $\text{sign}(u_{z1})$  accounts for the polarity of the seismic wave.

[12] The vertical polarization direction of an incoming wave at a seismic station ( $\psi_z$ ) can be estimated by

$$\psi_z = \cos^{-1} |u_{z1}|. \quad (3)$$

Here the vertical polarization direction indicates the apparent vertical incidence angle for a  $P$  phase. On the other hand, the  $SV$  wave has an angle  $\psi_z$  that is perpendicular to its vertical incidence angle. Also, the  $SH$  wave is polarized in a horizontal plane, and its  $\psi_z$  is  $\sim 90^\circ$ .

[13] The rectilinearity,  $\chi_{\text{rec}}$ , is given by [Vidale, 1986; Jepsen and Kennett, 1990]

$$\chi_{\text{rec}} = 1 - \frac{\lambda_2 + \lambda_3}{2\lambda_1}, \quad (4)$$

where  $\lambda_1, \lambda_2$ , and  $\lambda_3$ , are the eigenvalues for the covariance matrix in descending order ( $\lambda_1 \geq \lambda_2 \geq \lambda_3$ ). The rectilinearity measures the degree of polarization of a wave. The rectilinearity typically degrades with increase of reflections and scatterings. The estimates of rectilinearity are expected to be high for major direct phases, while they are low for background noises and multipath waves. Also, the planarity,  $\chi_{\text{pln}}$ , of a wave is given by

$$\chi_{\text{pln}} = 1 - \frac{2\lambda_3}{\lambda_1 + \lambda_2}. \quad (5)$$

The planarity measures the degree of confinement on a plane. Weakly polarized waves such as multiscattered waves have low planarities.

[14] The shear energy ratio can be measured from a ray-based  $LQT$  coordinate system. The  $L$  component is in the direction of incident  $P$  wave, the  $Q$  component is in the  $SV$  polarization direction that is perpendicular to the  $P$  direction, and the  $T$  component is the third component in the  $SH$  polarization direction. The  $L$  component is dominated by  $P$  energy, while the  $Q$  and  $T$  components are by  $SV$  and  $SH$  energies, respectively. The  $LQT$  records can be obtained from the event-based  $ZRT$ -component system [Jepsen and Kennett, 1990]:

$$\begin{bmatrix} L(t) \\ Q(t) \\ T(t) \end{bmatrix} = \begin{bmatrix} \cos \phi & \sin \phi & 0 \\ -\sin \phi & \cos \phi & 0 \\ 0 & 0 & 1 \end{bmatrix} \begin{bmatrix} Z(t) \\ R(t) \\ T(t) \end{bmatrix}, \quad (6)$$

where  $\phi$  is the vertical incidence angle of  $P$ , which corresponds to the  $\psi_z(P)$  in equation (3). The energy of direct shear waves is mainly recorded on the  $Q$  and  $T$  components.

[15] The shear energy ratio,  $R_S$ , is given by

$$R_S(t_n) = \frac{\sum_{i=0}^N [Q^2(t_{m_i}) + T^2(t_{m_i})]}{\sum_{i=0}^N [L^2(t_{m_i}) + Q^2(t_{m_i}) + T^2(t_{m_i})]}, \quad (7)$$

where  $N$  is the number of discrete times in a time window, and  $m_i$  indicates a discrete point of  $n + i - N/2$ . The magnitude of  $R_S$  is expected to be close to 1 for direct shear phases, 0 for direct compressional phases, and  $\sim 0.66$  for diffusive waves of which the energy is distributed evenly over the three components. We apply a 10 s time window for the polarization analysis.

#### 4. Waveform Features

[16] We examine broadband seismic records of the UNEs in the Balapan and the Nevada test sites. Figure 2 presents the seismic waveforms that are bandpass filtered between 0.5 and 2.5 Hz. The waveforms are similar between the array records. In Figure 3, we compare the waveforms between stacked records and single-event records at station KHC of the Czech Seismic Network (CZ).  $P$  waves are well observed at all distance ranges, while moderate amplitudes of  $S$  waves are observed in regional and far-regional distances (see Figure 4). The regional and far-regional records of both the Balapan and Nevada UNEs are dominated by strong  $Lg$  waves (stations WMQ, LZH, and HIA for the Balapan UNEs and stations PAS, PFO, ANMO, and COR for the Nevada UNEs).

[17] The phase composition in record sections for the UNEs appears to vary with frequency. Figure 5 shows the seismic waveform at station KHC for the Balapan UNEs.  $P$  waves are dominant at high frequencies and are relatively weak at low frequencies. On the other hand, Love and Rayleigh waves stand out at low frequencies (Figures 5a and 5b). Shear waves are observed weakly at low frequencies, while they are hardly observable at high frequencies.

[18] We examine low-frequency shear wave properties from teleseismic long-period records of two Balapan UNEs (the 18 October 1981 UNE and the 16 December 1984 UNE) (Figure 6). Love waves are observed at most stations, which suggests the presence of  $SH$ -type energy. Rayleigh and Love waves are separated over the radial and tangential components at most stations. This observation suggests that the observed long-period waves are hardly influenced by medium anisotropy. We also observe long-period shear waves on both radial and tangential components at various stations (e.g., stations KEV, ANTO, and CHTO for the 16 December 1984 UNE in Figure 6c). These observations imply that the observed shear waves are not simple  $SV$ -type waves but may be  $SV$ - $SH$  combined waves.

[19] The teleseismic phase composition of the Balapan UNEs differs from that of a nearby natural earthquake with a magnitude of  $m_b = 5.8$  and a focal depth of 10 km. Figure 7 presents seismic records of the earthquake. The magnitude of the earthquake is comparable to those of the Balapan UNEs. The seismograms of the earthquake display large amplitudes of  $S$  phases ( $S, SS, SSS$ ) in both radial and tangential components. The amplitudes of  $S$  waves from the earthquake are much stronger than those from the UNEs as seen in Figure 6. This observation suggests that teleseismic shear energy is radiated weakly from the UNEs.

[20] The composition of the teleseismic shear energy of the UNEs also differs from that of the regional shear energy. Regional seismograms are composed of waves traveling through either the crust or the mantle lid. Regional waves develop mainly from the energy radiated at large take-off

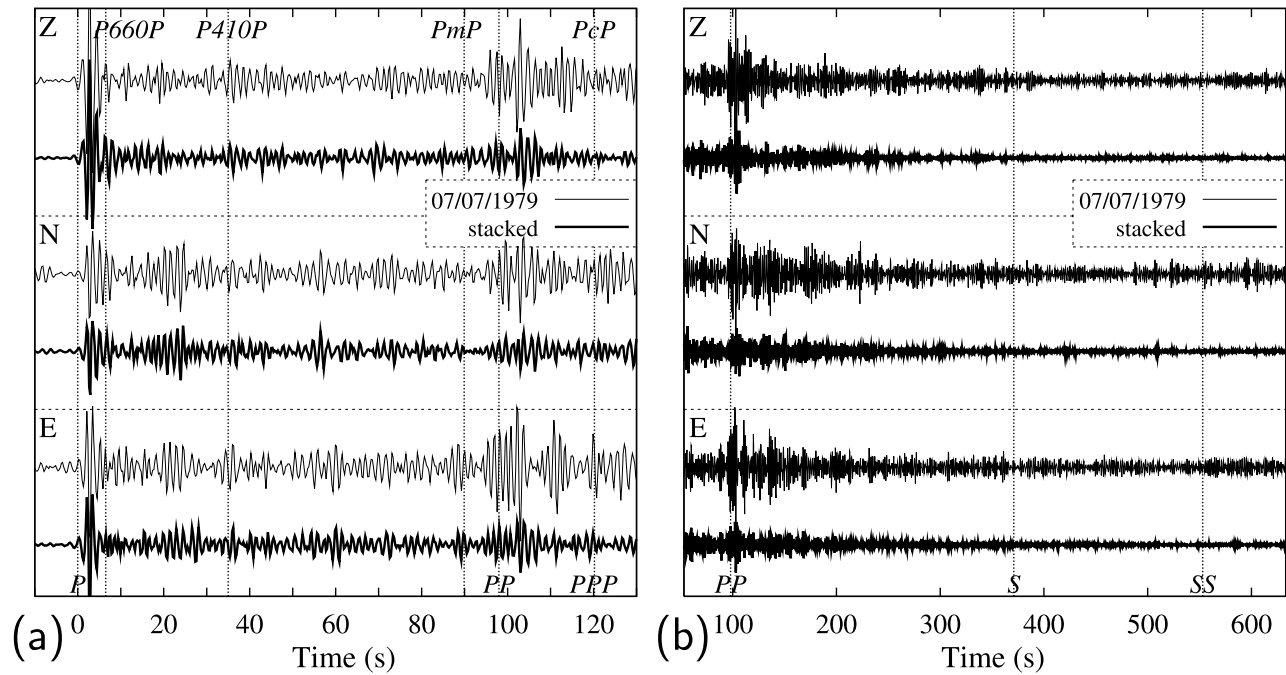


**Figure 3.** Comparisons of (a)  $P$ - and (b)  $S$ -wave record sections between a single UNE record and the stacked record at station KHC. Record sections are bandpass filtered between 0.5 and 2.5 Hz. The stacked record and the single UNE record display high correlation in the waveforms. Major shear phases such as  $S$ ,  $SS$  are not observed in the record sections.

angles from the sources compared to the energy-generating teleseismic waves. Figure 4 presents regional seismograms of two Balapan UNEs (the 12 October 1980 UNE and the 23 November 1976 UNE). The regional record sections display prominent mantle-lid shear waves and crustally guided shear waves (see also record sections of stations PAS and PFO in Figure 2b). Such strong regional shear waves are often observed from UNEs in other regions [e.g., *Hong et al.*, 2008]. The observation of strong regional shear waves suggests that the shear energy may be excited more at high take-off angles.

[21] It is well known that a significant amount of shear energy is observed in regional wave trains from UNEs [e.g., *Hong and Xie*, 2005]. However, the shear energy becomes weak with increasing frequency, while  $P$  energy is consistently strong. This feature allows us to use the amplitude ratios between  $P$  and  $S$  waves from regional records for discrimination of nuclear explosions from natural earthquakes [e.g., *Walter et al.*, 1995; *Taylor*, 1996; *Xie*, 2002; *Ringdal et al.*, 2002; *Fisk*, 2006; *Hong and Rhie*, 2009].

[22] We measure  $S/P$  amplitude ratios to understand the distance-dependent variation of shear-energy composition in seismic records of UNEs. Shear waves typically prevail in horizontal components at teleseismic records. Thus, we use root-mean-square amplitudes of three component records to take into account both  $P$  and  $S$  energy. We analyze the pairs of the first-arrived  $P$  and  $S$  waves in this study. The arrival times of  $P$  and  $S$  waves are calculated based on the 1-D global average model (ak135) of *Kennett et al.* [1995]. Since the  $P$  and  $S$  waves are expected to share the same (or very close) raypaths from the source to a receiver, the geometrical

spreading effect is naturally corrected in the calculation of  $S/P$  amplitude ratio. Also, we employ a constant frequency band for all distances to avoid discriminative frequency-dependent attenuation. As a result, only the phase-dependent wave responses to inherent medium properties along raypaths and source regions are reflected in the  $S/P$  amplitude ratio.

[23] We now measure the  $S/P$  amplitude ratios. Considering the frequency contents of regional and teleseismic waves from the UNEs (see Figure 3), we analyze the  $S/P$  ratios in a

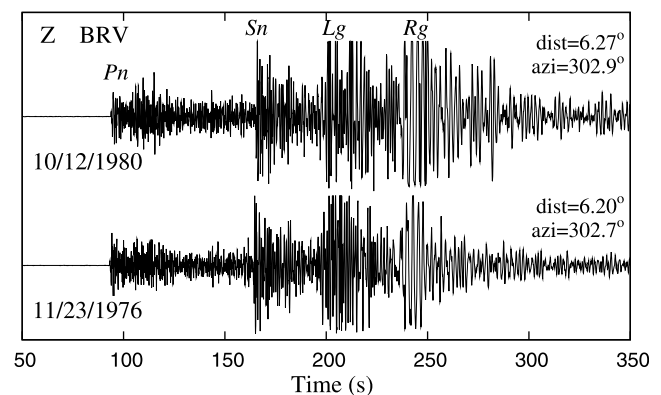


**Figure 4.** Regional seismograms of the 12 October 1980 and 23 November 1976 Balapan UNEs. The distances and azimuths from events to stations are presented. Crustally guided shear waves ( $Lg$ ) and strong mantle-lid shear waves ( $Sn$ ) are observed.

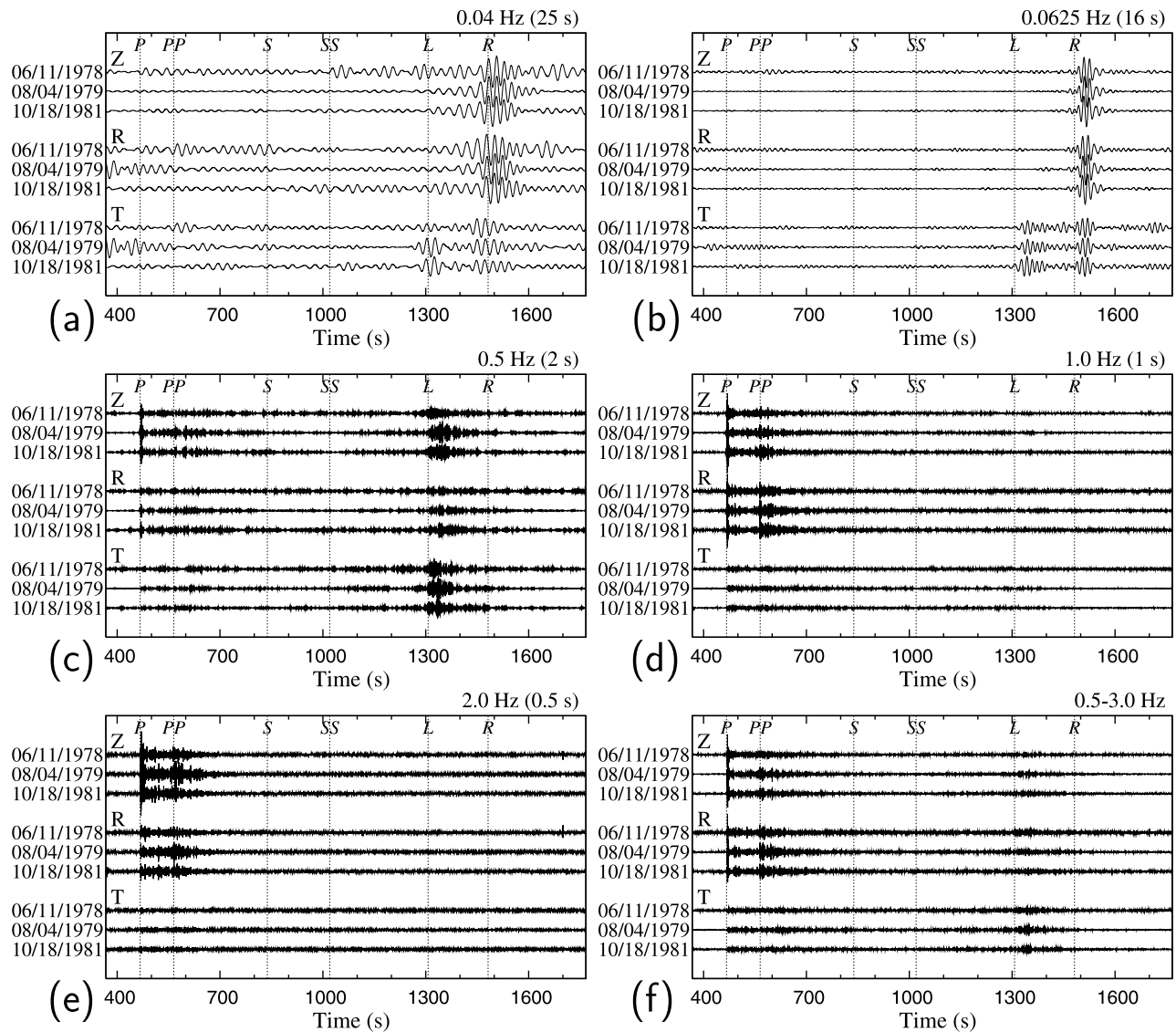


**Figure 5.** Variation of phase compositions of teleseismic records with change of frequency: (a) 0.04 Hz, (b) 0.0625 Hz, (c) 0.5 Hz, (d) 1.0 Hz, (e) 2.0 Hz and (f) 0.5–3.0 Hz. Three Balapan UNE records at station KHC are analyzed (11 June 1978, 4 August 1979, 18 October 1981). Characteristic dispersive Love and Rayleigh waves are observed at lower frequencies (a and b). High-frequency  $Lg$  waves are observed in the frequencies around 0.5 Hz (c). Body-wave phases are mostly observed at high frequencies (d and e). Shear wave phases ( $S$ ,  $SS$ ) are rarely observed unlike the  $P$  phases (f).

frequency band of 1–2 Hz. Figure 8 shows the  $S/P$  amplitude ratios for the Balapan and Nevada UNEs. The  $S/P$  amplitude ratios are given by around 1–3 in regional distances ( $<10^\circ$ ) and become close to 0 in teleseismic distances.

[24] We compare the shear-energy composition of the UNEs with that of natural earthquakes. To calculate the representative  $S/P$  ratios of earthquakes, we choose 12 shallow-focus earthquakes in various regions. The events have various focal mechanisms (Table 3 and Figure 9). The event magnitudes are 5.5–6.0, which are comparable to those of the UNEs. Seismic data are collected from global networks to reduce the effects of azimuth-dependent radiation patterns of seismic waves. A total of 1257 three-component broadband seismic records from GSN stations is used. The  $S/P$

ratios of the earthquakes are estimated in the same frequency range of 1–2 Hz.

[25] Figure 10 presents a comparison of  $S/P$  amplitude ratios between UNEs and earthquakes. In general, the  $S/P$  ratios for both UNEs and earthquakes appear to decrease with distance at regional and far-regional distances and are observed to be nearly constant at teleseismic distances. The  $S/P$  ratios of regional UNEs, however, display relatively large variations compared to those of regional earthquakes. The large variation of  $S/P$  ratios in regional UNEs may be associated with small number of observations that can be influenced by receiver-site geology, anisotropic raypaths, and inhomogeneous source excitations. However, we find that such large variation is not observed in teleseismic

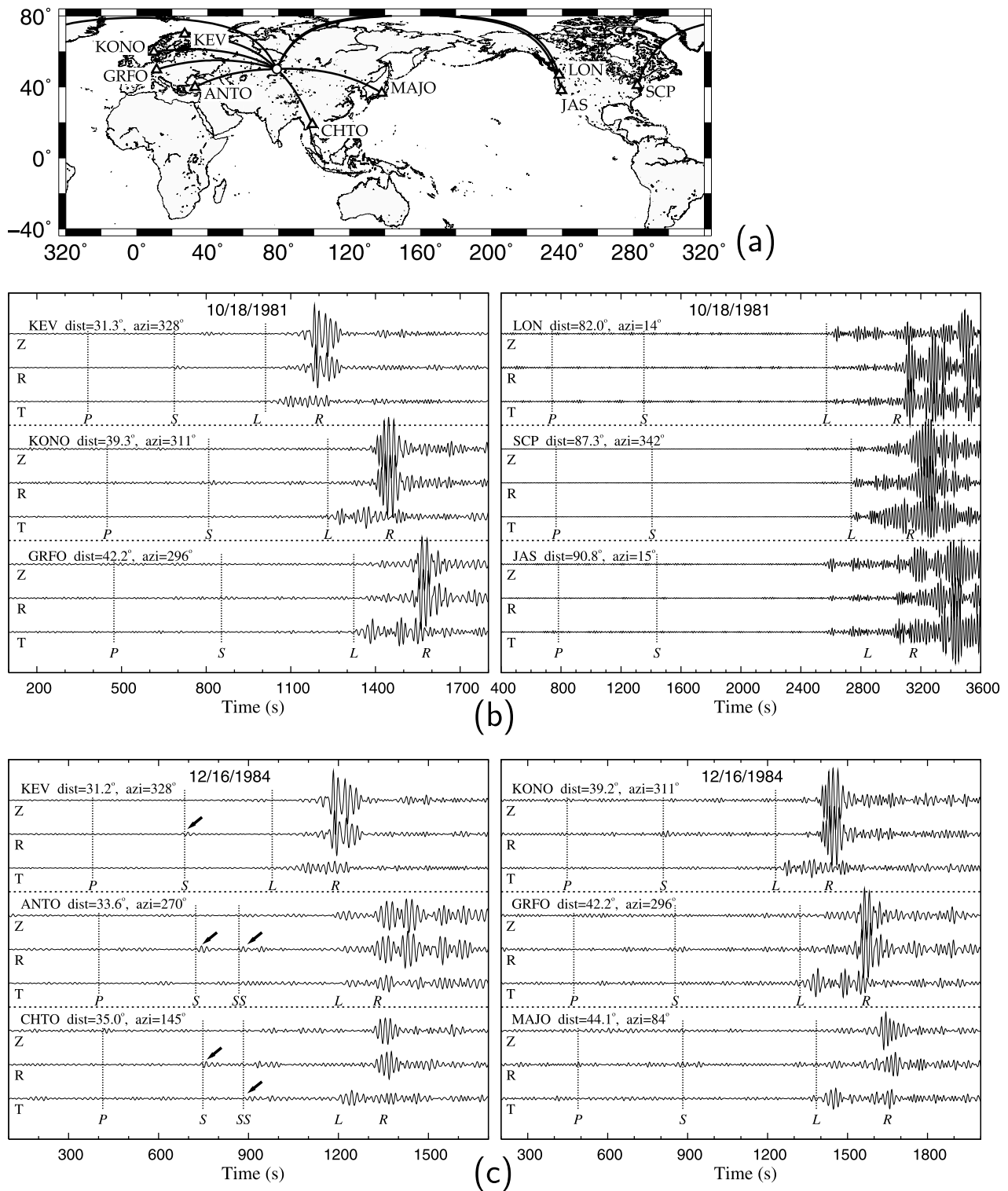


**Figure 6.** Long-period record sections of two Balapan UNEs at global teleseismic stations. (a) Location map of the UNEs and stations, (b) record sections of the 18 October 1981 UNE and (c) record sections of the 16 December 1984 UNE. The waveforms are bandpass filtered between 0.05 and 0.1 Hz. Theoretical arrival times of *P*, *S*, Love (*L*) and Rayleigh waves (*R*) are marked. The distances and azimuths from events to stations are denoted. Love waves are clearly observed in tangential components of most stations. Surface waves are dominant in every record section. Shear waves are observed rarely in most records. Weak shear energy is occasionally observed on the radial components at some teleseismic distances (arrows on the 16 December 1984 UNE records of stations CHTO and ANTO). The shear energy is much weaker than that of a natural earthquake at comparable distances (see Figure 7).

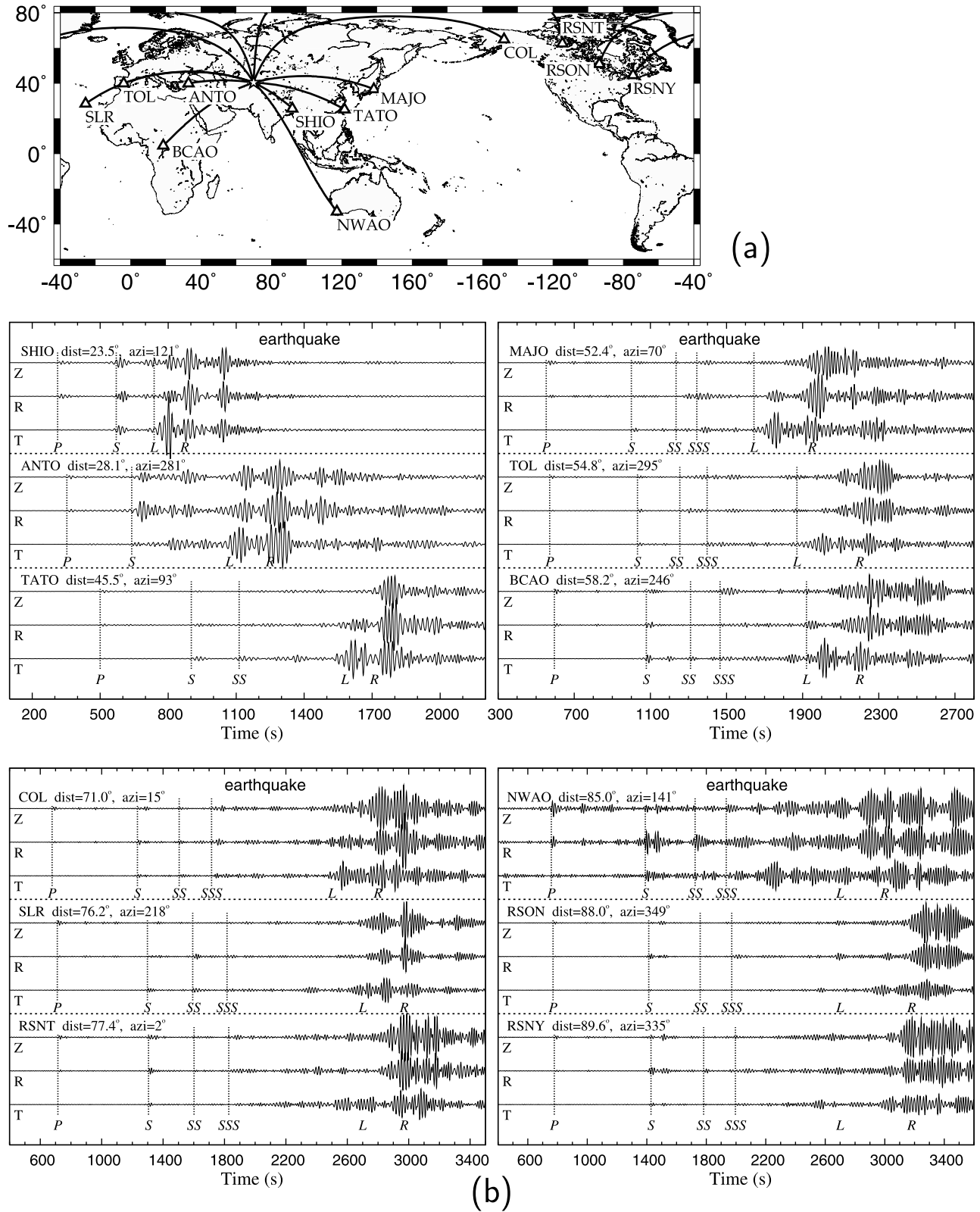


**Figure 7.** Telesismic records of a natural earthquake with magnitude of  $m_b = 5.8$  and focal depth of 10 km: (a) location map and (b) record sections. The record sections are bandpass filtered between 0.05 and 0.1 Hz. The distances and azimuths from events to stations are denoted. Theoretical arrival times of major phases are marked. Strong shear phases are observed in every record section.

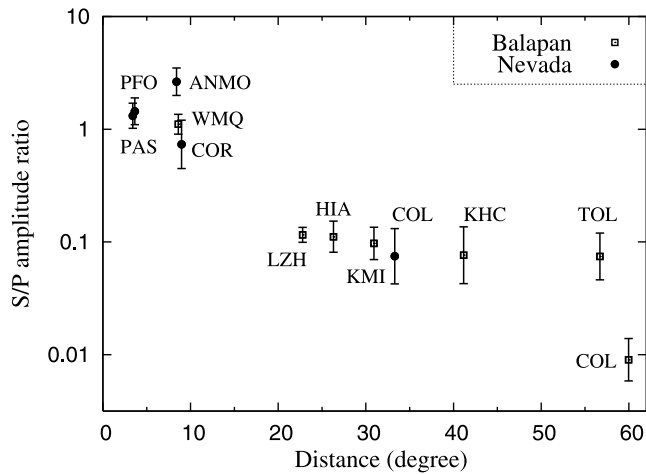


**Figure 8.**  $S/P$  amplitude ratios of the seismic records for the Balapan (open squares) and Nevada (filled circles) UNEs. The standard deviations of the estimated  $S/P$  ratios are presented with error bars. The  $S/P$  ratios appear to be conformable between the Balapan and Nevada UNEs. The names of stations are annotated. The  $S/P$  ratios are high at regional distances ( $<10^\circ$ ), and decrease to around 0.1 at far-regional and teleseismic distances. The  $S/P$  ratio decreases significantly at a distance around  $60^\circ$ .

UNEs. The teleseismic  $S/P$  ratios of earthquakes are about three times larger than those of the UNEs at teleseismic distances between  $20^\circ$  and  $60^\circ$ . We find an exceptionally low  $S/P$  ratio in a teleseismic UNE at a distance of around  $60^\circ$ .

[26] The dominant factors responsible for the large variation in  $S/P$  ratios of regional UNEs are not constrained with the observations. However, the observations suggest that considerable amount of shear energy is excited from regional UNEs although the regional shear energy from the UNEs can be weaker than that from earthquakes. The clear level difference in teleseismic  $S/P$  ratios between UNEs and earthquakes suggests that the teleseismic  $S/P$  ratios can be effectively used for discrimination of UNEs from earthquakes.

## 5. Shear Wave Features in the Source Region

[27] A source array frequency-wave number (F-K) analysis is applied to the record sections of the spatially clustered Balapan and Nevada UNEs. The source array F-K analysis allows us to investigate the phase composition of seismic wavefields in the source region. Thus, the analysis enables us to identify the dominant phases in the source region. Seismic records of seven broadband stations (WMQ, KMI, LZH, KHC, TOL, HIA, COL) for the Balapan UNEs and five broadband stations (COR, PAS, PFO, ANMO, COL) for the Nevada UNEs are analyzed (see Figure 1).

[28] The waveform records of the Balapan and Nevada UNEs are aligned to a  $P$  travel-time curve based on the 1-D global velocity model of Kennett *et al.* [1995]. The time corrections made by the phase alignment is presented in Tables 1 and 2. The magnitudes of the time shifts are much smaller than 0.5 s for most seismograms, except for the records of station KHC for the 4 July 1976, 5 September

1977, 11 June 1978, 4 August 1979, and 12 October 1980 Balapan UNEs and the record of station COL for the 26 March 1992 Nevada UNE.

[29] Considering the regional waveform records at station BRV that do not display any significant time difference [see Hong and Xie, 2005], the large time differences in the record sections of station KHC may be associated with recording time errors. The recording time error may be possibly introduced during digitization of the analog seismic records. Similarly, the time difference of the 26 March 1992 Nevada UNE at station COL appears to be related to a recording time error in comparison to the time differences at other stations.

[30] The source array analysis is applied to a set of event records with at least five seismograms. We use spatially clustered UNEs as source arrays of which apertures and array-component intervals are sufficiently small enough to resolve coherent regional and teleseismic waves. The frequency band for the source array analysis is slightly modified by station around 0.5–0.8 Hz considering the array apertures, array-component intervals, and frequency contents of incoming waves.

[31] It is noteworthy that the source arrays are based on events occurring at different origin times. Thus, only the waves developing consistently over time are enhanced in the analysis, while inconsistent seismic noise is suppressed. The enhancement of signature increases with the number of array components. Array analysis is based on normalized slowness power spectra that display the relative strengths of phases in given wavefields. The energy of a particular phase is identified from the magnitude of the slowness power spectrum in the azimuthal direction.

[32] The array analysis is based on single source array records. The array components are clustered in space. Thus, every source array component shares similar ray paths to the station. As a result, path effects such as attenuation and anisotropy are equally reflected over all array records. The raypaths can be assumed to be the same except in the region around the source arrays. Any effects that the waves experience on paths outside the source region are not reflected by this method. Thus, the slowness power spectra from a source array analysis reflect the phase properties in the source region.

[33] The ray parameter of a seismic phase is proportional to the take-off angle from the source. Seismic waves with

**Table 3.** Source Parameters of 12 Shallow Earthquakes Used in This Study for  $S/P$  Ratio Measurement<sup>a</sup>

Date	Time	Lat. ( $^\circ$ )	Long. ( $^\circ$ )	Dep. (km)	Mag.	$N$
02/21/2007	11:05:09.2	36.44	41.04	10	5.7	107
02/25/2007	20:47:25.4	-28.57	-176.56	6	5.9	27
03/09/2007	07:27:31.2	-11.42	66.25	10	5.8	53
03/10/2007	17:03:36.3	74.21	8.75	10	5.9	169
03/15/2007	06:07:58.0	3.94	126.44	9	5.8	43
03/25/2007	13:57:57.5	38.49	20.37	9	5.5	220
04/04/2007	21:40:18.7	30.92	141.67	9	5.6	168
04/12/2007	18:24:52.4	-61.17	160.37	10	5.7	19
04/13/2007	18:24:18.3	-34.88	-108.86	10	5.9	132
05/05/2007	08:51:36.3	34.23	81.87	10	6.0	185
05/16/2007	08:56:13.1	20.57	100.75	1.3	5.8	100
05/20/2007	14:18:18.8	27.14	88.35	10	5.6	34

<sup>a</sup>The number of stations ( $N$ ) is given.

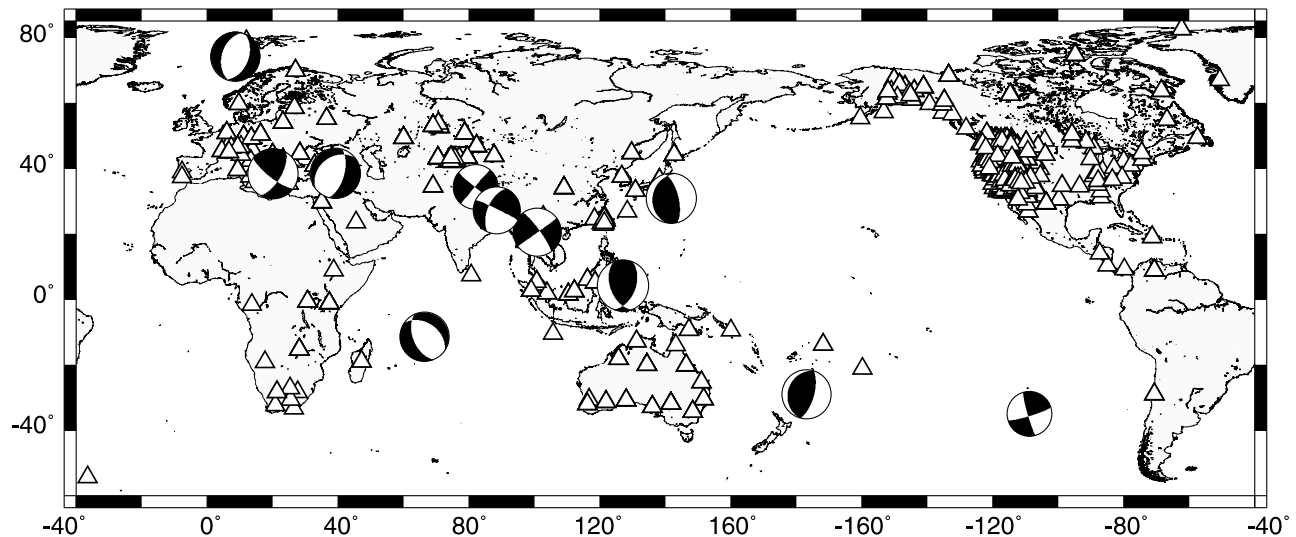


**Figure 9.** Map of 12 shallow earthquakes analyzed to measure  $S/P$  amplitude ratios. The focal mechanism solutions are presented on the locations of events. The locations of stations are marked with triangles.

low ray parameters dive deep into the Earth's interior, and return to the Earth's surface at long distances. Thus, the epicentral distance decreases with take-off angle. We examine the variation of seismic radiation patterns with distance, which allows us to infer the variation of seismic energy with the take-off angle. Also, investigation of radiated energy dependent on the azimuth enables us to infer the azimuthal variation of seismic energy.

[34] The phase compositions at the theoretical arrival times of  $P$  and  $S$  are presented in Figures 11 and 12. The F-K analysis reveals that  $S$  energy is identified on the slowness power spectra at most stations despite contamination with noise.  $S$  energy is mostly observed on the horizontal components in teleseismic distances. Regional stations present  $S$  energy in vertical components, which may be due to large incidence angles. The observation of shear waves in the source array records suggests that the shear energy is excited in a consistent manner at every detonation. We also find that the separation of shear energy over radial and tangential components is not uniform among stations.

[35] Shear waves in the Balapan UNE records at stations KHC and COL are mostly seen on the radial components. On the other hand, other stations display shear energy on both horizontal components (Figure 11). Such nonuniform shear-energy distribution is also observed in the Nevada UNE records. The Nevada UNE records at station PFO display dominant shear energy mostly on the radial components (Figure 12b), while those at station ANMO present the shear energy only on the tangential components (Figure 12c).

[36] Shear waves can be decomposed into  $SV$  and  $SH$  components. The  $SV$  and  $SH$  can be diminished depending on the radiation patterns, which typically appear in either four-lobed or two-lobed patterns for single fault systems (Figure 13). The observed  $S$  energy division over radial and tangential components as function of azimuth, however, does not show the typical radiation patterns. This nonuniform shear-energy distribution suggests that the polarization direction of shear waves from the UNEs varies with azimuth.

[37] We determine horizontal polarization directions of shear waves by searching for directions in which the maximum shear energy is observed. We quantify the  $S$  energy in the source array records that are rotated for given azimuthal angles from  $0^\circ$  to  $360^\circ$ . Here, the  $S$  energy corresponds to the slowness power spectra with  $S$  phase velocity in the direction of the great circle path. Figures 14 and 15 present the shear-energy variation of every station as function of the azimuthal angle. The shear energy appears to vary with the azimuthal angle in a sinusoidal periodic pattern at most stations.

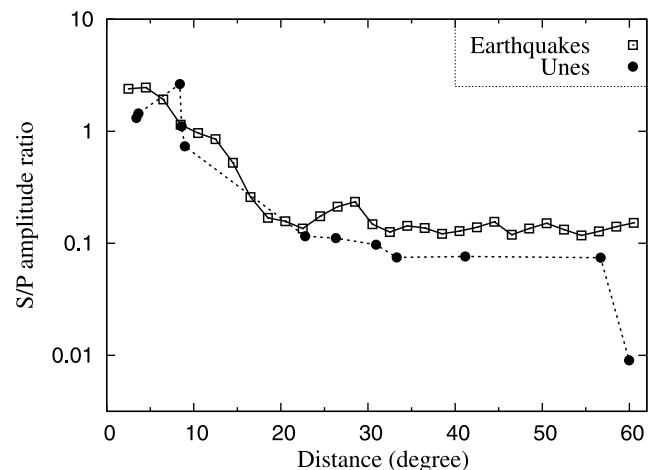


**Figure 10.**  $S/P$  amplitude ratios of natural earthquakes (open squares) and comparison with those of the UNEs (filled circles). The  $S/P$  amplitude ratios appear to be similar between the earthquakes and the UNEs at distances up to  $\sim 22^\circ$ . The  $S/P$  amplitude ratios of the earthquakes are estimated to be about three times larger than those of the UNEs at teleseismic distances. The difference becomes much significant at a distance around  $60^\circ$ .

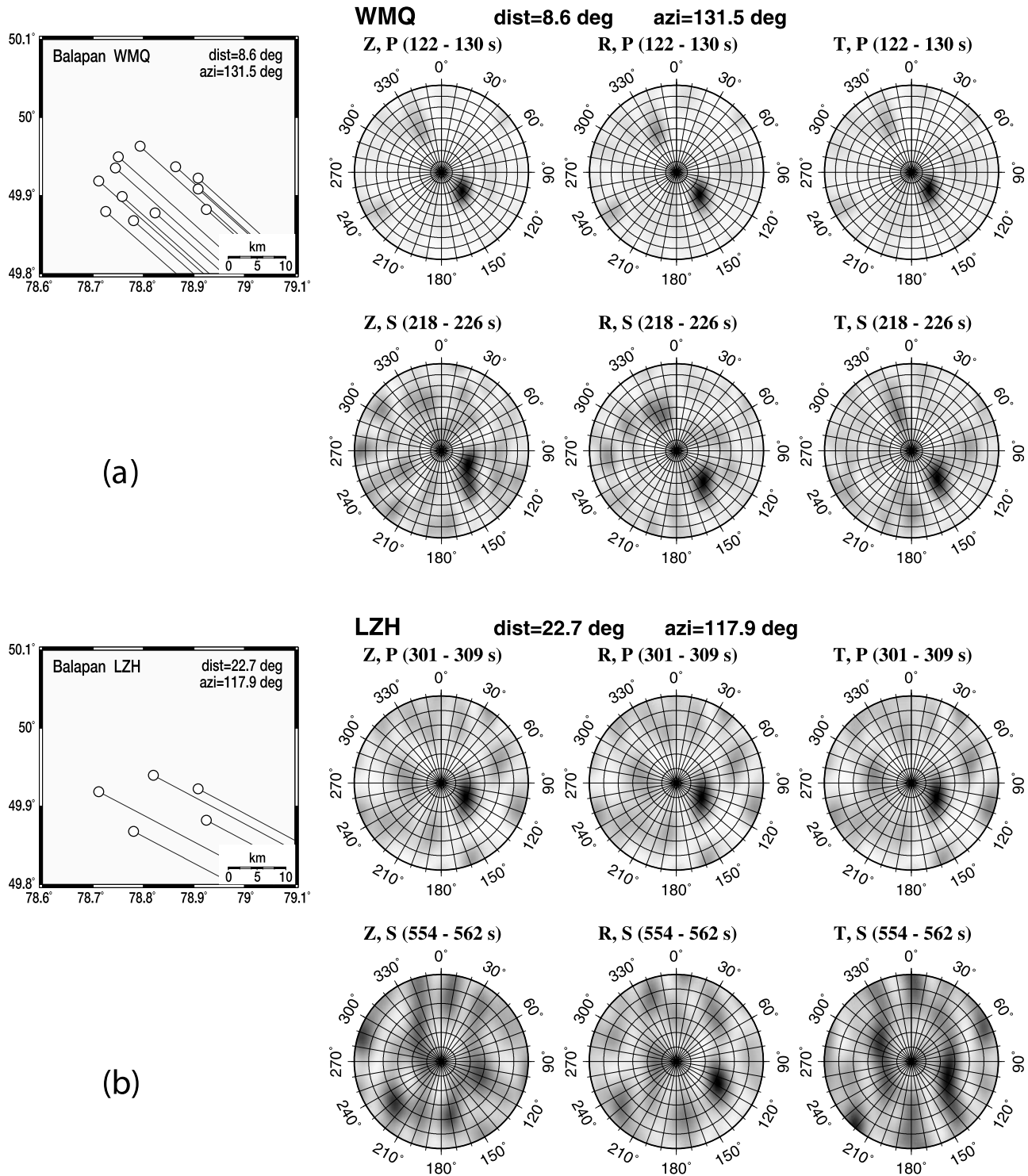


**Figure 11.** Source array geometry and slowness power spectra (vertical (Z), radial (R), tangential (T)) of *P* and *S* waves from the Balapan UNEs: stations (a) WMQ, (b) LZH, (c) HIA, (d) KMI, (e), KHC, (f) TOL, and (g) COL. The distances and azimuths are denoted. The great circle paths are presented on the map. The waveform time windows are denoted. The slowness grid interval is 0.05 s/km. Coherent *P* and *S* energy is observed. Some multiple peaks develop in the *S*-wave slowness power spectra due to influence of scattered waves and noises. *S* energy is nonuniformly divided into two horizontal components, and the energy division is different by station.

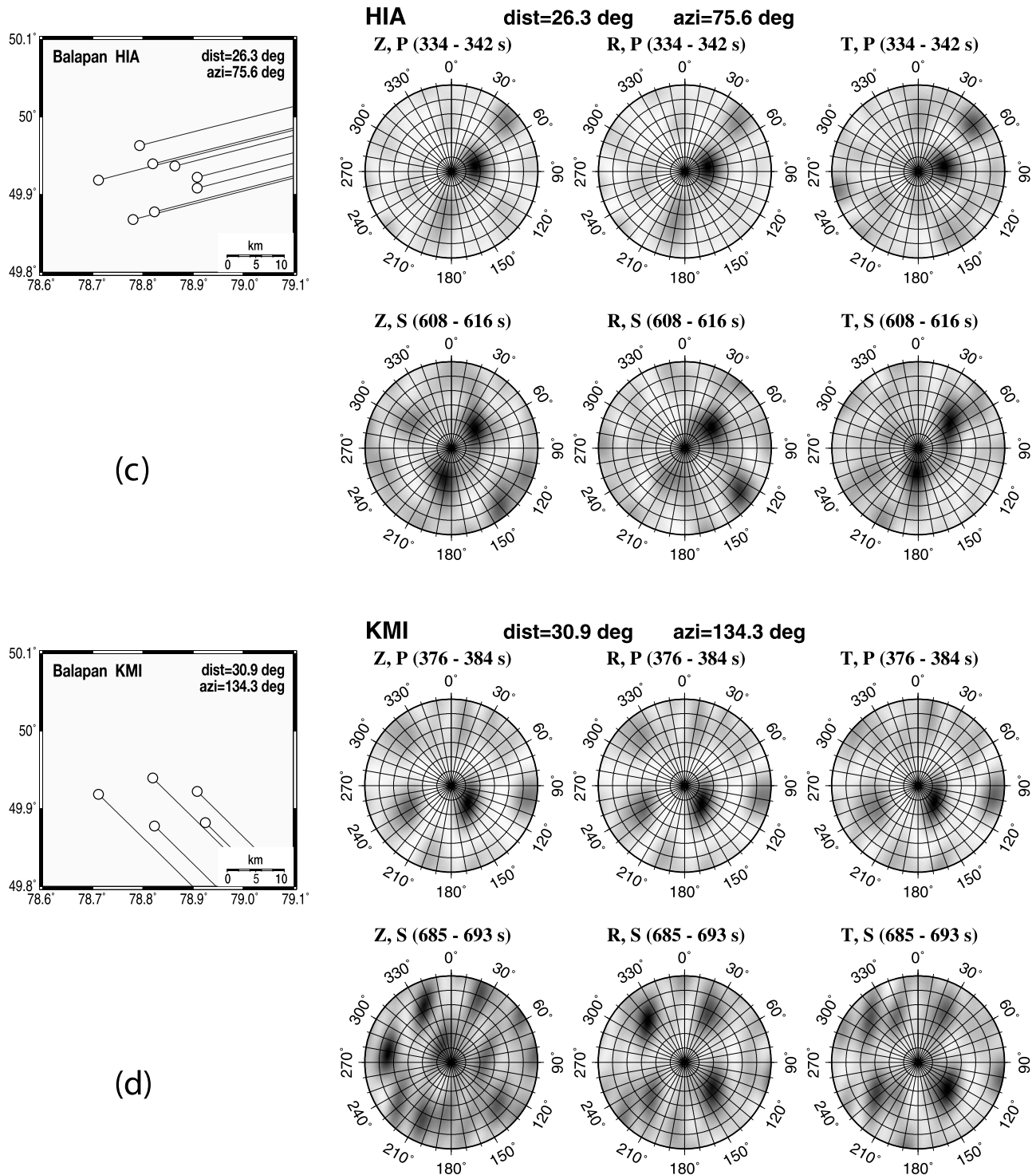
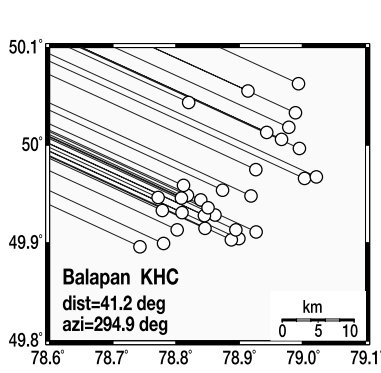


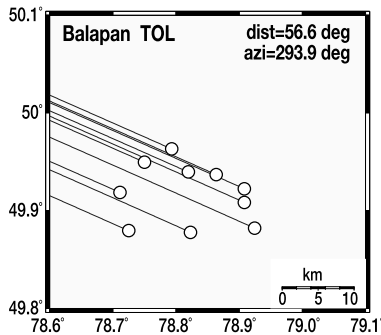
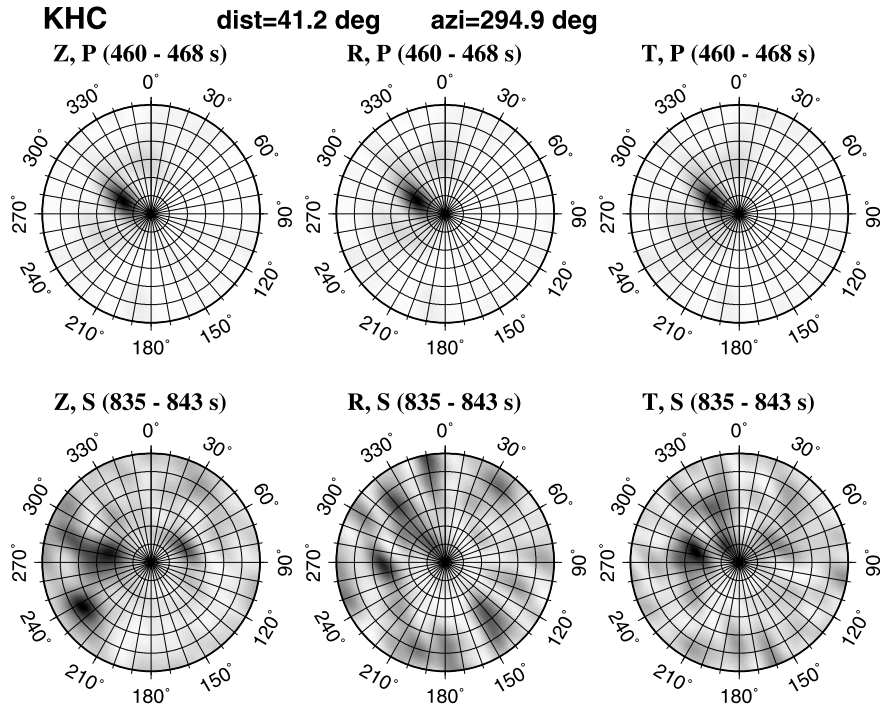
Figure 11. (continued)

[38] The azimuthal angles for the maximum shear energy seem to be consistent among the stations located in similar great circle directions (see, Figures 14h and 15f). Stations TOL, KHC, and LZH for the Balapan UNEs present similar polarization directions and the same for stations WMQ and KMI (Figure 14h). However, these polarization directions

change with azimuths. The observation of consistent polarization directions among stations with different distances in similar directions of great circle paths implies that the local heterogeneity in 3-D Earth structures rarely affects the shear wave polarization. The azimuth-dependent shear wave polarization suggests that the shear energy is not



(e)



(f)

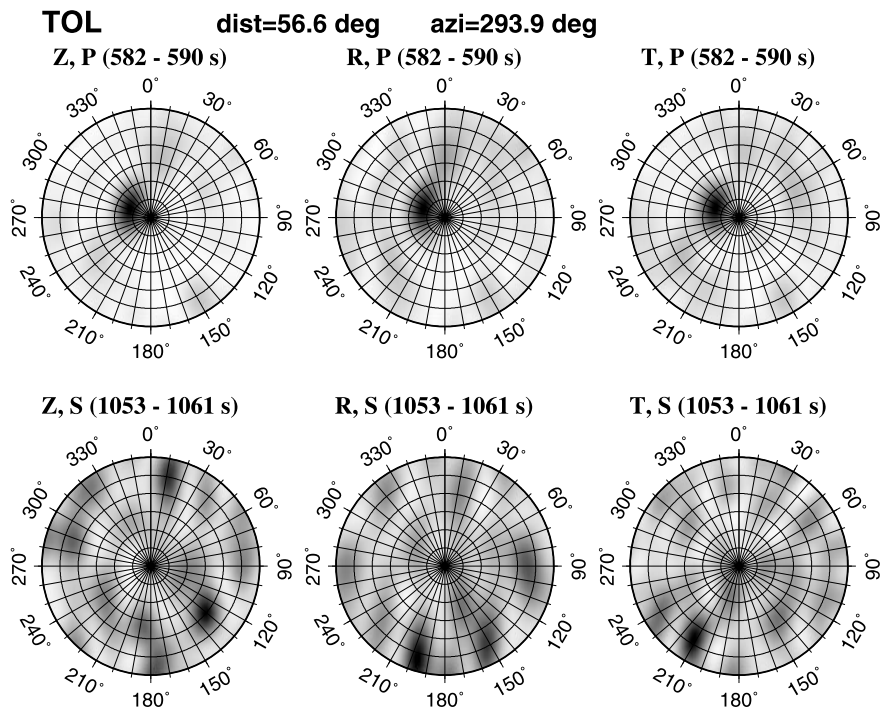


Figure 11. (continued)

radiated from a single common source but may be from multiple sources with nonuniform strengths.

### 6. Teleseismic Shear Wave Composition

[39] The source array analysis as described in the previous section allows us to resolve time-invariant coherent shear

waves in the source region. In this section, we examine the presence of shear energy, including both time-variant and time-invariant energy. The time-variant energy can be investigated by examining each record section using polarization methods (see section 3.2). These methods allow us to discriminate between *P* and *S* phases and to assess the amount of shear energy included in each record section. We analyze the Balapan UNE records of station KHC of the

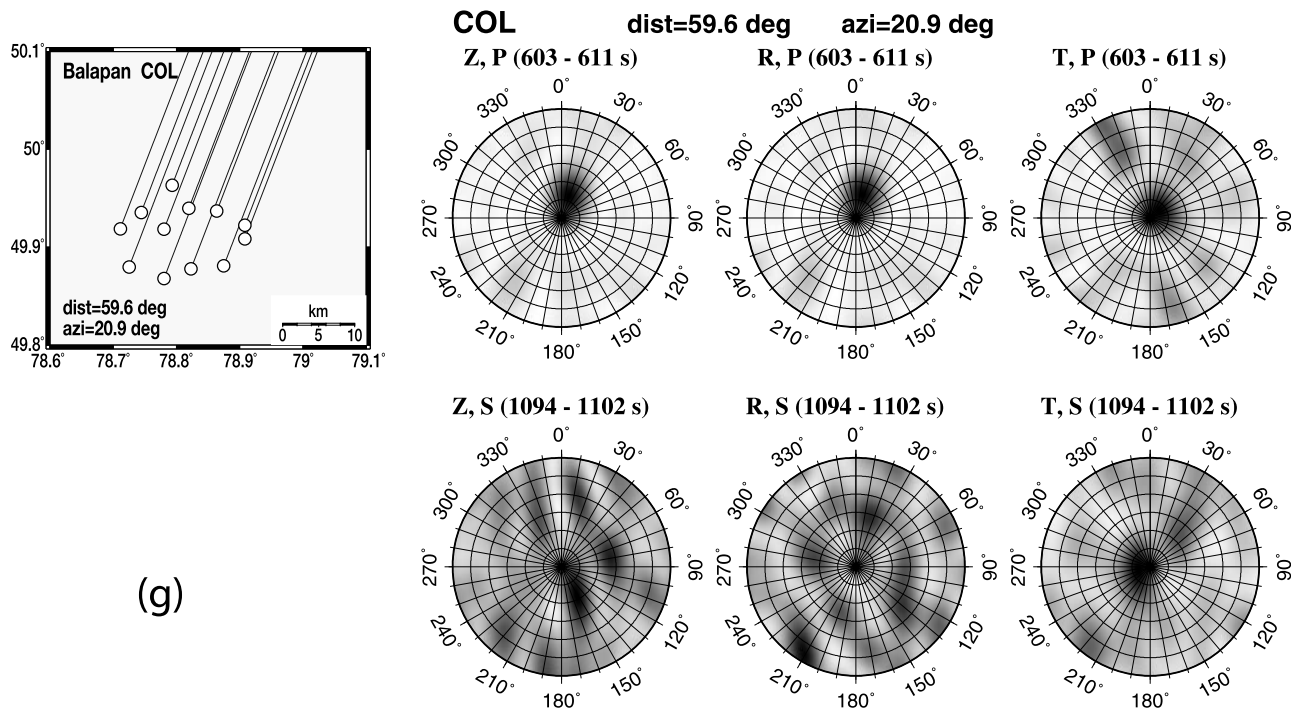


Figure 11. (continued)

Czech Seismic Network (CZ). The record sections are composed of 30 three-component broadband seismograms.

[40] Dilatational  $P$  waves are excited from UNEs. Thus, direct  $P$  and surface-reflection  $P$  phases (e.g.,  $PP$  and  $PPP$ ) are polarized in the direction of propagation from the source to the receiver. The direction corresponds to the azimuth,  $\varphi$ . Also, polarization directions of interface-reflection  $P$  phases and wavetype-coupled  $P$  waves are given by either  $\varphi$  or  $\varphi + 180^\circ$ , depending on the impedance contrasts across the interfaces.

[41] Shear waves can be divided into two components, vertically polarized ( $SV$ ) and horizontally polarized shear energy ( $SH$ ). The horizontal polarization angle,  $\psi_h$ , of  $SV$  is given by either  $\varphi$  or  $\varphi + 180^\circ$ . On the other hand,  $SH$  waves are horizontally polarized in the direction perpendicular to the propagation direction. Thus,  $\psi_h$  of  $SH$  is given by  $\varphi \pm 90^\circ$ .

[42] Figures 16 and 17 present the horizontal and vertical polarization directions, rectilinearity, and planarity of  $P$  and  $S$  wave trains. The horizontal and vertical polarization directions of direct  $P$  phases ( $P$  and  $PP$ ) are estimated consistently (Figure 16). The vertical polarization directions of  $P$  and  $PP$  are estimated at  $\sim 25^\circ$  and  $\sim 35^\circ$  from the vertical axis, respectively. In addition, direct  $P$  phases exhibit high rectilinearity and planarity. Shear waves coupled with  $P$  waves on the interfaces between laterally stratified layers are  $SV$ -type waves. Their horizontal polarization directions correspond to either positive or negative azimuth.  $SH$ -type shear waves can be generated by wave-type coupling of  $P$  waves on the interfaces with topography.

[43] The horizontal polarization directions of wavelets at the theoretical arrival times of  $S$  and  $SS$  are estimated to be about  $60^\circ$  and  $240^\circ$  (Figure 17). The estimated vertical polarization directions are distributed over the entire range

of  $0^\circ$ – $90^\circ$ . The observation of horizontal polarization directions suggests that the energy at the  $S$  and  $SS$  arrival times is mainly composed of either  $P$  or  $SV$ -type shear waves. However, the wide distribution of vertical polarization angles (i.e., vertical incidence angles) suggests that the observed energy is rarely composed of coherent phases but are rather mixed with various scattered waves. Such waves may originate from multiple reflections or scatterings in the crust.

[44] The rectilinearity and the planarity are close to 1 at  $PP$  arrival times and are reduced to around 0.4–0.9 after the  $PP$  phase, even at the expected arrival times of  $S$  and  $SS$ . The rectilinearity and planarity are estimated to be constant over time. The relatively high values of rectilinearity and planarity in the expected  $S$ -wave portion suggest that the constitutional phases are polarized on a single plane. Furthermore, the constant rectilinearity and planarity values in the  $S$  wave trains between  $PP$  and  $SS$  phases indicate no significant change in the compositional energy such as significant  $S$ -energy arrivals.

[45] Major  $P$  phases have low shear energy ratios ( $R_s$ ) of  $\sim 0.02$  for  $P$ , and 0.1–0.4 for  $P410P$ ,  $PmP$ , and  $PP$  (Figure 16e). The shear energy ratios appear to increase gradually with time in the wave train between  $PP$  and  $SS$  arrival times, which causes  $R_s$  to vary in a wide range of 0.3–0.85. No significant change in shear energy ratios is observed in the wave trains around the expected arrival times of  $S$  and  $SS$  (Figure 17e). These observations suggest that the  $S$ -wave portion is mainly composed of scattered waves which may be originated from  $P$  waves. Thus, it appears that direct  $S$  waves are rarely or weakly included in the wave train. Nevertheless, shear wave signatures are seen in the surface waves (Figure 5c).

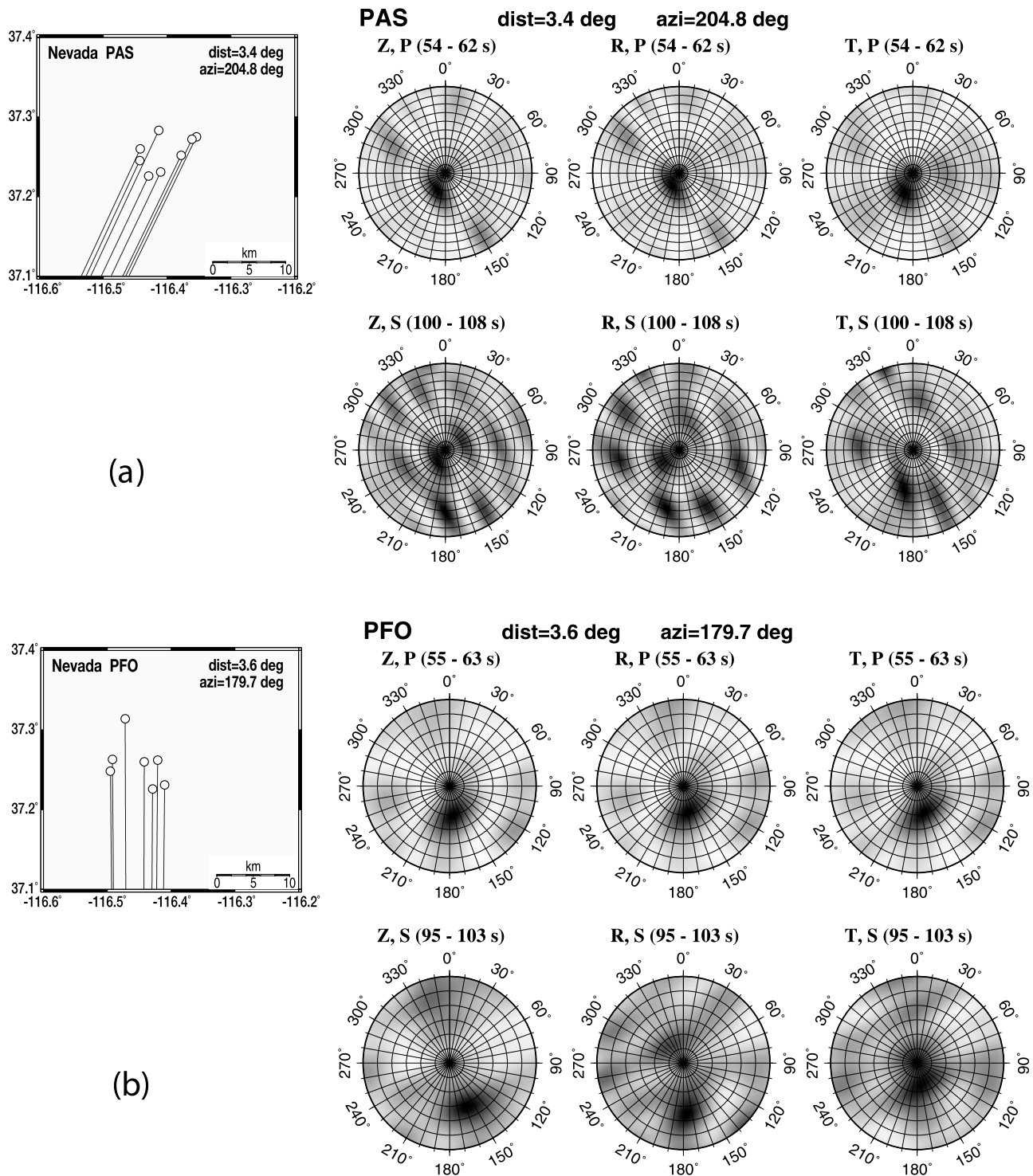


**Figure 12.** Source array geometry and slowness power spectra (vertical (Z), radial (R), tangential (T)) of P and S waves from the Nevada UNEs: stations (a) PAS, (b) PFO, (c) ANMO, (d) COR, and (e) COL. The distances and azimuths are denoted. The great circle paths are presented on the map. The analyzed time windows are denoted. The slowness grid interval is 0.05 s/km. Coherent P and S waves are observed.

[46] The weak teleseismic shear waves suggest that shear energy is hardly radiated at small take-off angles from the source (Figure 18). This inference agrees with teleseismic observations of shear phases from UNEs [e.g., Nuttli, 1969;

Wallace et al., 1985]. It is intriguing to observe consistent *Lg* development even at teleseismic distances. This is because *Lg* develops from constructive interferences of postcritically reflected shear waves in the crust, which

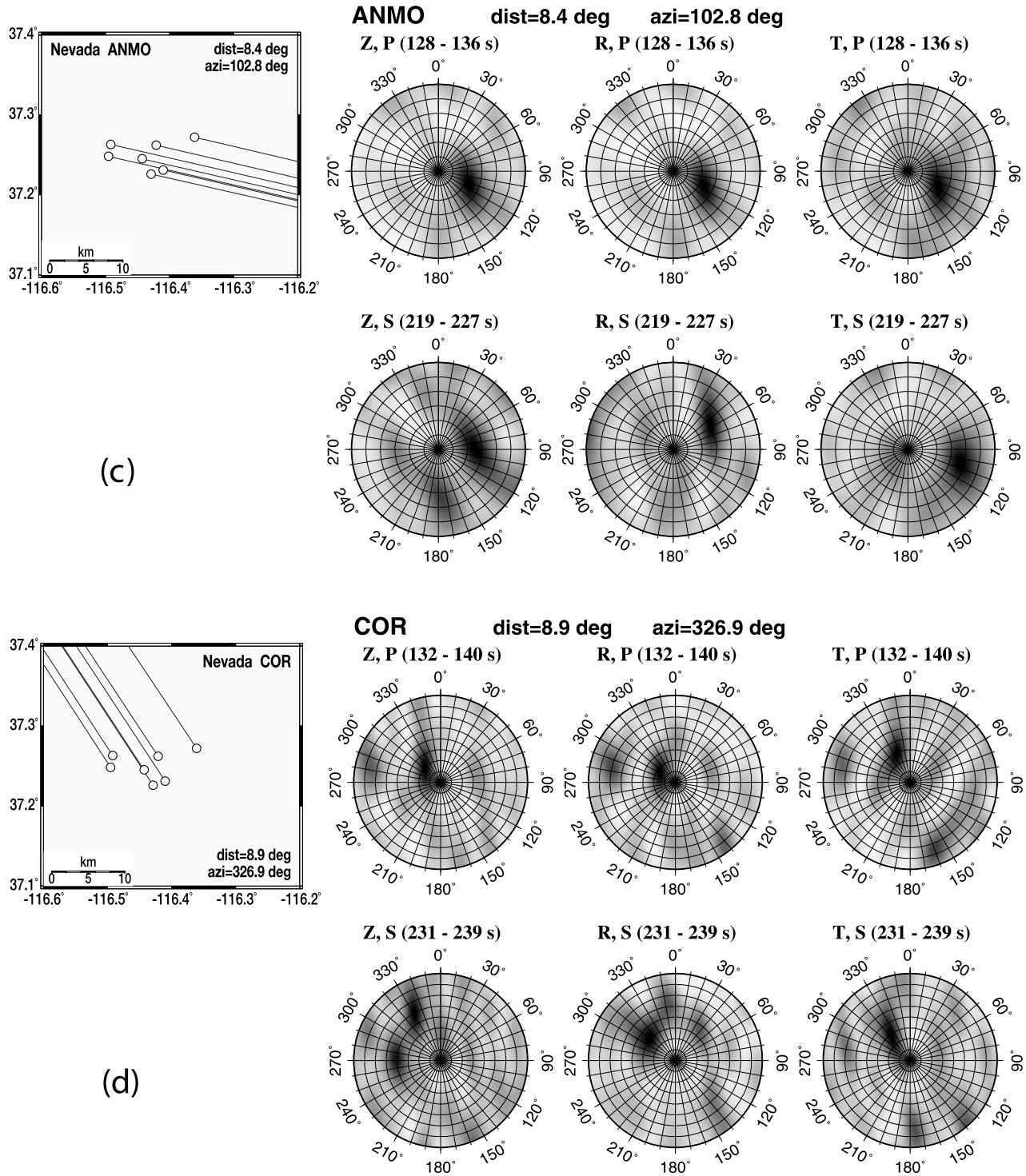


Figure 12. (continued)

enables crustal-guided transmission with relatively low loss of energy even to teleseismic distances.

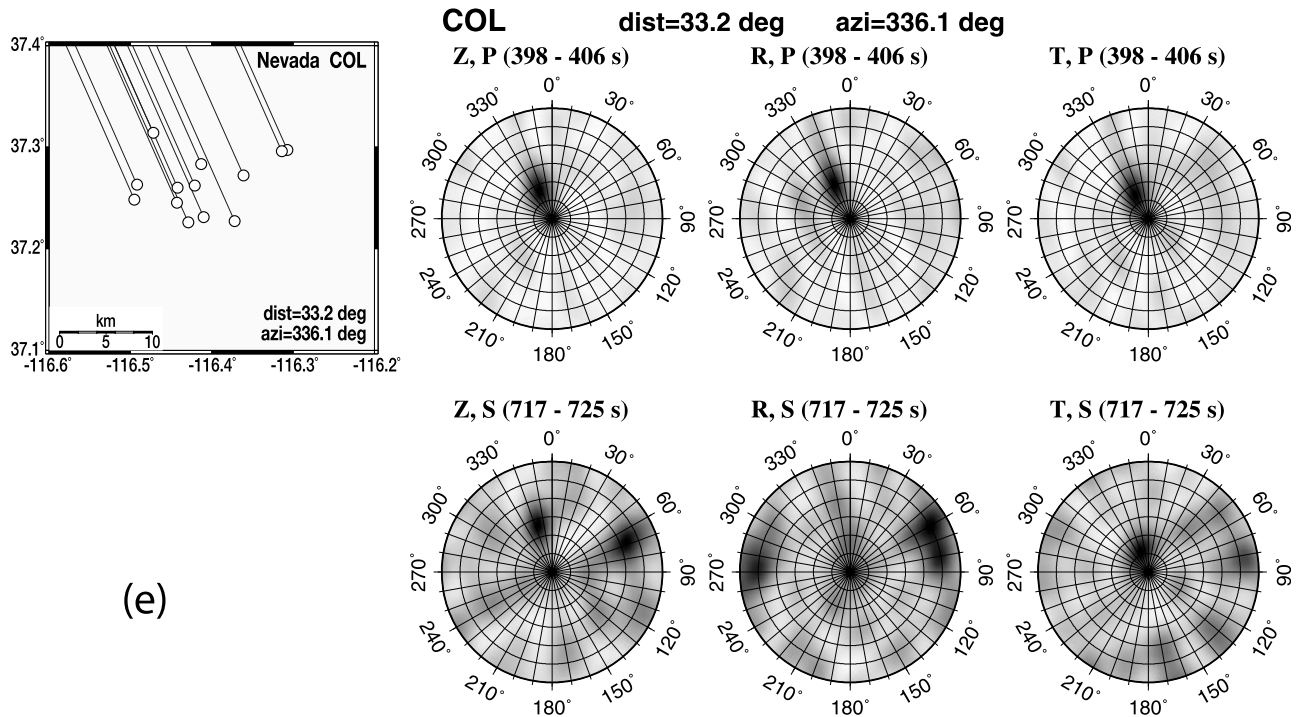
**7. Implications for Shear Wave Excitation Mechanism**

[47] Various mechanisms have been proposed for the explanation of shear wave excitation from UNEs. We

examine the observed shear wave features and test them with respect to the proposed shear wave excitation mechanisms.

**7.1. Rg (Rayleigh Wave) to S Scattering**

[48] This mechanism explains the development of shear waves as a result of scatterings of Rg waves on crustal heterogeneities [e.g., Gupta et al., 1992; Myers et al., 1999].



(e)

Figure 12. (continued)

The  $Rg$  wave is the fundamental-mode Rayleigh wave. When  $Rg$  waves are scattered from regional or local heterogeneities (e.g., surface topography, lateral variations in seismic properties), they are coupled into various modes of surface waves and body waves. Scattered waves originated from  $Rg$  are well observed in the regional seismic coda [Hong et al., 2006]. The radiation patterns of coupled surface waves and body waves are dependent not only on the mode or wave type, but also the geometry of the heterogeneity. Anisotropic geometry of heterogeneities in the Earth causes radiation of the coupled shear waves in various directions. Thus, the radiation directions depend on both the incidence direction and the geometry of heterogeneity. As a result, coupled shear waves developing from  $Rg$  scattering are expected to be observed in teleseismic records.

7.2.  $S^*$

[49] When a  $P$ -wave source is close to a seismic discontinuity such as the free surface, the  $P$  wave is wavetype-coupled into a strong nongeometric impulsive  $SV$  wave on the boundary. This shear wave is called  $S^*$  wave [e.g., Gutowski et al., 1984; Vogfjörð, 1997]. The magnitude of  $S^*$  is inversely proportional to the distance between the discontinuity and the source. The  $S^*$  is strong particularly when the discontinuity is the free surface. Thus, a shallow explosive source excites strong  $S^*$  on the free surface. It is known that the  $S^*$  wave is radiated only for take-off angles greater than the critical angle (Figure 19). The critical angle,  $\psi_d$ , is given by [Vogfjörð, 1997]

$$\psi_d = \sin^{-1}\left(\frac{\beta_0}{\alpha_0}\right), \tag{8}$$

where  $\alpha_0$  and  $\beta_0$  are  $P$ - and  $S$ -wave velocities in the source region.

[50] The take-off angle dependency of the  $S^*$  energy is consistent with observations of strong shear waves at regional distances but weak shear waves at teleseismic distances (see section 6). Teleseismic body waves develop from energy radiated at small take-off angles, in which  $S^*$  energy is rarely or weakly radiated (i.e.,  $\theta < \psi_d$ ).

[51] The strong excitation of  $S^*$  energy at large take-off angles ( $\theta > \psi_d$ ) supports the observation of prominent  $Lg$  waves that develop due to postcritical reflections of shear waves on the Moho. This crustally guided shear energy can be transported to teleseismic distances along high  $Q$  paths, with fractional energy loss due to geometrical spreading (Figure 20).

[52] The observation of high-frequency  $Lg$  energy in both regional and teleseismic distances is consistent with the  $S^*$  mechanism. When the shear wave velocity in the source region is low, the critical reflection angle on the Moho is estimated small.  $S^*$  energy can be easily trapped in the crust due to a decrease of the critical angle. This theoretical expectation agrees with a field observation of Hong and Xie [2005] where strong shear waves are excited from a low-velocity region.

[53] The  $S^*$ , however, is an  $SV$ -type shear wave. Thus, shear phases originating from  $S^*$  are expected to be observed in radial and vertical components if they are present. Since seismic waves are incident near vertically to teleseismic stations, the  $SV$ -type shear waves should be observed mainly on the radial components. This explains the observation of shear waves mainly on the radial components (see Figure 6). However, the strong  $Lg$  and Love energy in tangential records is not well explained by the  $S^*$

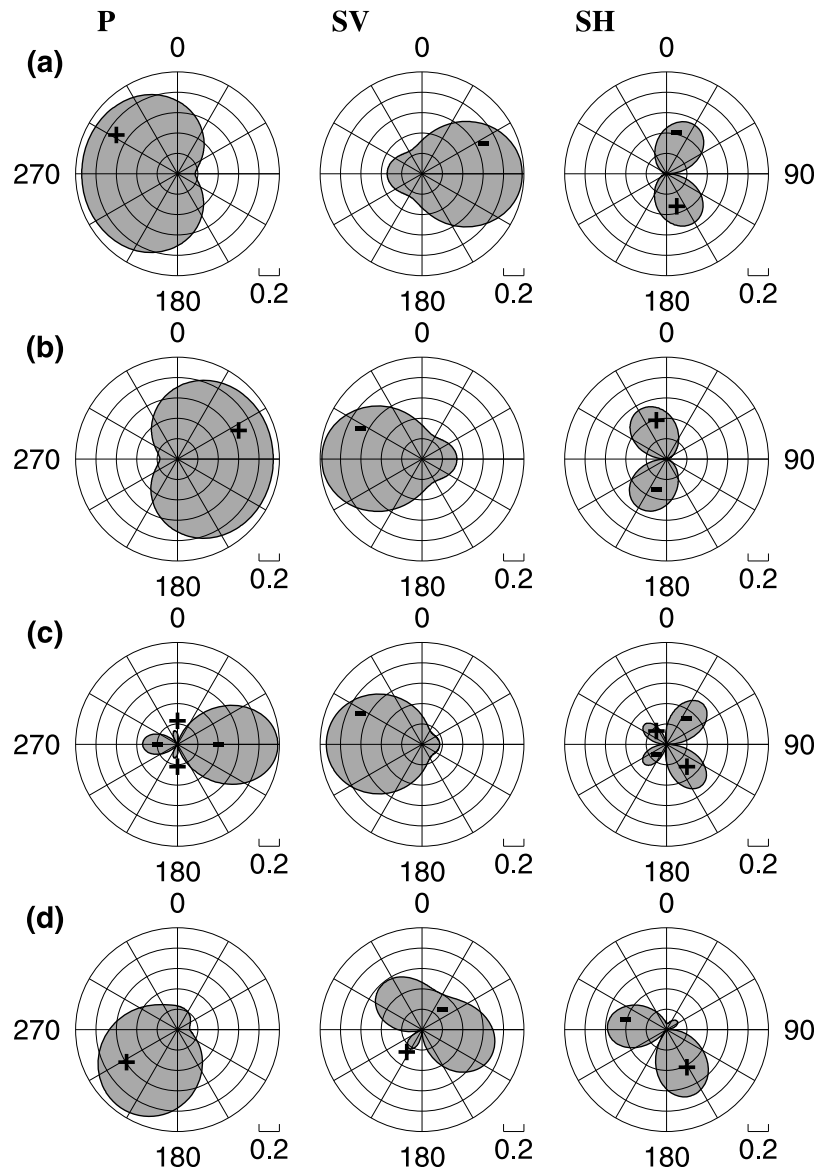


**Figure 13.** Radiation patterns of  $P$  (left),  $SV$  (middle), and  $SH$  (right) waves for four different dip-slip models. (a) The dip ( $\delta$ ) of the fault plane is  $60^\circ$ , the rake ( $\lambda$ ) is  $90^\circ$ , and the take-off angle ( $i_\xi$ ) is  $25^\circ$ . (b)  $\delta = 30^\circ$ ,  $\lambda = 90^\circ$ , and  $i_\xi = 25^\circ$ . (c)  $\delta = 60^\circ$ ,  $\lambda = 90^\circ$ , and  $i_\xi = 70^\circ$ . (d)  $\delta = 60^\circ$ ,  $\lambda = 45^\circ$ , and  $i_\xi = 25^\circ$ . The radiation patterns are presented as function of the difference in angle between the station azimuth and the fault strike. The radiation patterns are highly dependent on the fault geometry and the slip direction.

mechanism, which requires strong  $SV$ -to- $SH$  wavetype coupling. Furthermore, the azimuthally anisotropic polarization directions of shear waves and the inconsistent shear energy distribution between radial and tangential components do not agree with the  $S^*$  mechanism.

### 7.3. Rock Cracking and Tectonic Release

[54] This mechanism ascribes the shear wave excitation to cracking or rupturing of rocks by a shock wave from a nuclear explosion [e.g., Massé, 1981]. The medium above the source is conically cracked due to explosion. Tectonic releases are associated with rock cracking. It is known that an explosive source with rock cracking can be described

with a compensated linear vector dipole (CLVD) source [e.g., Toksöz *et al.*, 1971; Patton and Taylor, 1995]. Seismic waves associated with tectonic releases are observed in regional and teleseismic distances [e.g., Wallace *et al.*, 1985; Burger *et al.*, 1986; Walter and Patton, 1990; Ekström and Richards, 1994; Levshin and Ritzwoller, 1995].

[55] In particular, the tectonic-release signature is well observed in the analyses of surface waves [Brune and Pomeroy, 1963; Aki and Tsai, 1972; Archambeau, 1972; Helle and Rygg, 1984; Day *et al.*, 1987; Harkrider *et al.*, 1994]. Patton [1991] reported that the fault systems associated with tectonic release vary with the detonation sizes; explosions with detonations greater than 300 kt produce

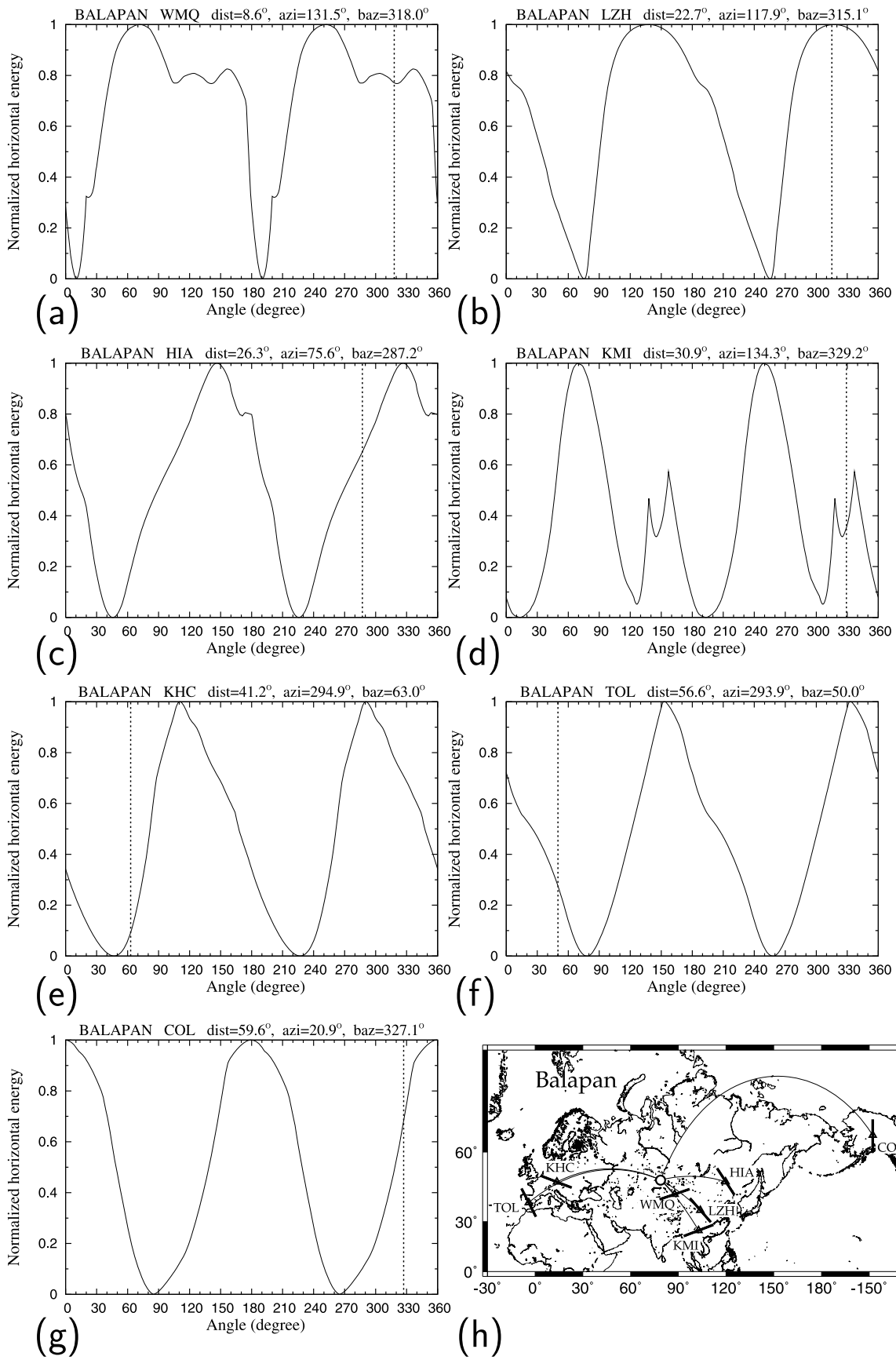
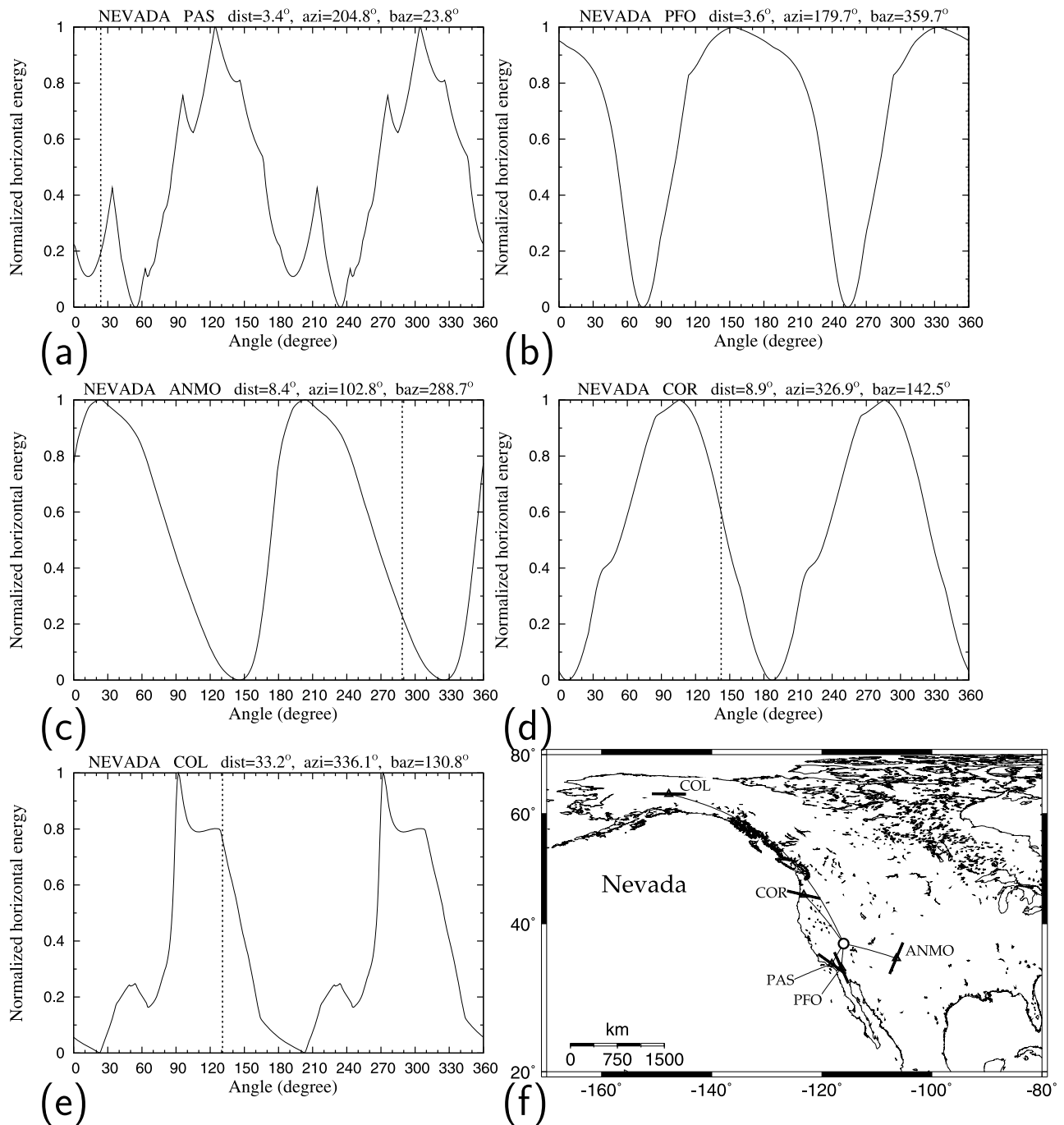


Figure 14



**Figure 15.** Normalized shear energy variation with rotation angle for the Nevada UNEs: stations (a) PAS, (b) PFO, (c) ANMO, (d) COR, (e) COL, and (f) the shear-energy variation as function of rotation angle. The back azimuths are marked with dotted lines. The direction of the maximum shear energy corresponds to the polarization direction of the shear wave. The polarization directions are different among stations.

**Figure 14.** Normalized shear energy variation with rotation angle for the Balapan UNEs: stations (a) WMQ, (b) LZH, (c) HIA, (d) KMI, (e) KHC, (f) TOL, (g) COL, and (h) the shear-energy variation as function of rotation angle. The back azimuths are marked with dotted lines. The direction of the maximum shear energy corresponds to the polarization direction of the shear wave. The polarization directions appear to vary with the azimuths between the UNEs and stations. The polarization directions are consistent among stations in the same (or similar) great circle directions.



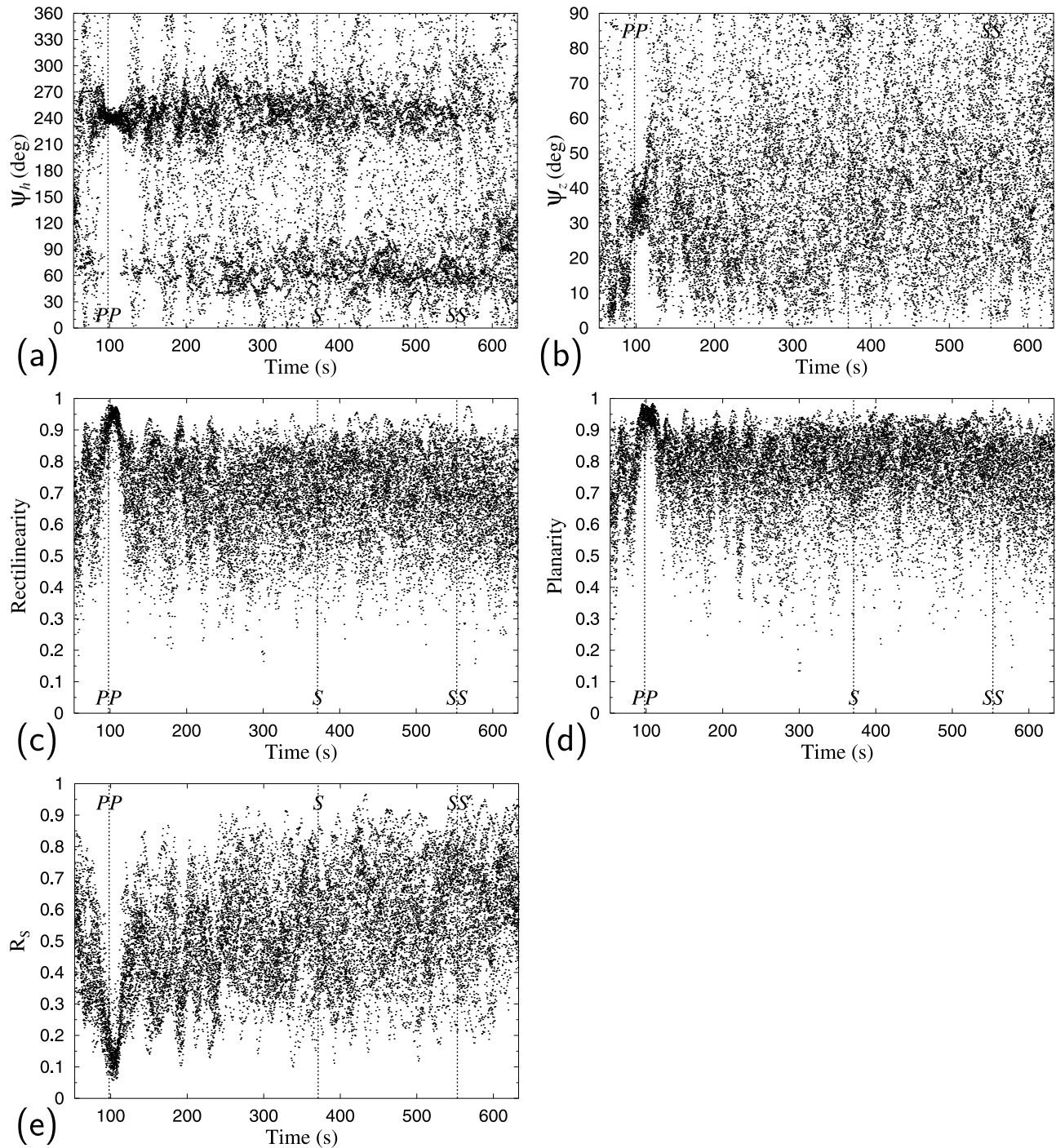


**Figure 17.** Polarization analyses of  $S$ -wave portions in the Balapan UNE records of station KHC: (a) horizontal polarization direction, (b) vertical polarization direction, (c) rectilinearity, (d) planarity, and (e) shear energy ratio.  $PP$  phase exhibits the signatures of a direct phase such as consistent horizontal and vertical polarization directions and high rectilinearity and planarity. The broad variation of vertical polarization directions and the ordinary rates of rectilinearity, planarity and shear energy ratio at the expected onset times of  $S$  and  $SS$  suggest rare inclusion of shear energy.

and Richards, 2002, p108]. The radiation pattern changes significantly with the fault parameters and the slip direction. The magnitude of shear wave radiated from a single dip-slip segment changes with the direction (Figure 13). Such single

fault systems cannot satisfy the azimuthal variation of polarization directions of shear waves in Figures 14 and 15.

[57] An alternative model may be that such dip-slip or strike-slip dislocations (rock cracking) develop in conical

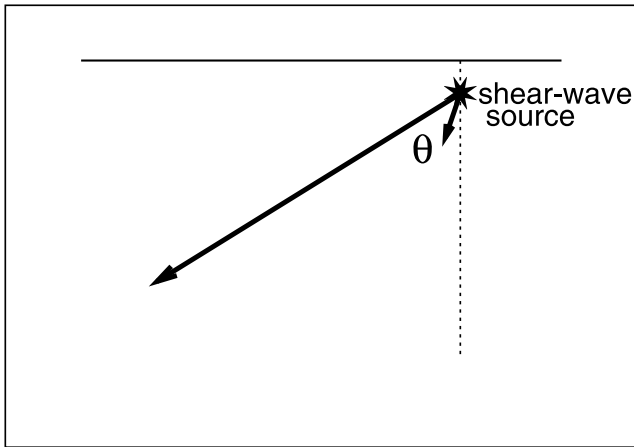


**Figure 18.** Schematic description of shear-energy radiation from the source. The strong *Sn* and *Lg* phases at regional distances (Figure 4) suggest strong excitation of shear waves at large take-off angles ( $\theta$ ). The rare (or weak) teleseismic shear energy implies rare (or weak) radiation of shear waves at small take-off angles.

shapes with respect to hypocenters [Massé, 1981]. In this model, the total energy radiated from the source region corresponds to an integration of seismic energy from each fault segment over a ring of conical dip-slip (or strike-slip) fault system. Thus, the shear energy may vary with azimuth due to the difference in relative influence of each fault segment. Also, the shear energy may vary with the take-off angle due to inhomogeneous energy radiation depending on the fault geometry. The extinction of teleseismic shear energy may be explained by the vertical radiation-angle (take-off angle) dependence. The high energy at intermediate take-off angles in Figure 13 supports the strong observation of *Lg* phase at regional and teleseismic distances.

**7.4. Spall**

[58] Spall is a widely observed spatial deformation in UNE sites, which illustrates a phenomenon of vertical opening and closing of tensile cracks due to shock waves

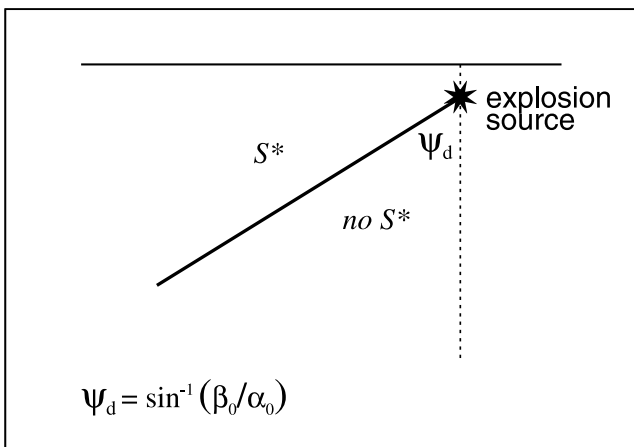


**Figure 19.** Angular distribution of *S\** energy. The *S\** energy is radiated at the take-off angles greater than  $\psi_d$ .

[e.g., Eisler and Chilton, 1964; Stump, 1985; Day and McLaughlin, 1991]. The vertical opening and closing of crack causes excitation of strong horizontal shear wave components in the vertical direction. If this effect is strong enough, shear waves are expected to be observed at teleseismic distances. The tensile crack model produces azimuthally isotropic shear waves [Stump, 1985; McLaughlin et al., 2004]. However, these features do not agree with the observed azimuthal variation of polarization directions of shear waves.

**8. Discussion and Conclusions**

[59] We analyzed the regional and teleseismic records of the Balapan and Nevada UNEs. Strong monotonic *Lg* energy is observed at both regional and teleseismic distances. Dispersive Love and Rayleigh waves are observed at frequencies below 0.1 Hz. Unlike the prominent appearance of teleseismic *P* phases, shear waves (*S*, *SS*) are weakly observed. Weak teleseismic shear energy has been investigated using a source array F-K analysis that is based on the records of spatially clustered events. The observation of coherent shear energy with consistent polarity suggests that the shear energy is excited in the same manner at every detonation.

[60] The source array analysis shows that the polarization directions of shear waves vary with azimuths. This observation suggests azimuthally anisotropic radiation of shear energy, which may be a result of multiple shear wave excitation sources. We find that considerable amount of shear energy is observed from regional UNE records. The strength of regional shear energy appears to vary with station, which may be a result of combined effects of receiver-site geology, anisotropy along ray paths and inhomogeneous radiation from the sources. On the other hand, we find significantly low shear energy in teleseismic UNE records, implying weak radiation of shear energy at low take-off angles.

[61] The observational features of regional and teleseismic records are examined with respect to various shear wave excitation mechanisms, which include *S\**, tectonic release (rock cracking), *Rg*-to-*S* scattering, and spall. It appears that the tectonic-release model with a conical faulting system agrees well with both the regional and teleseismic observations.

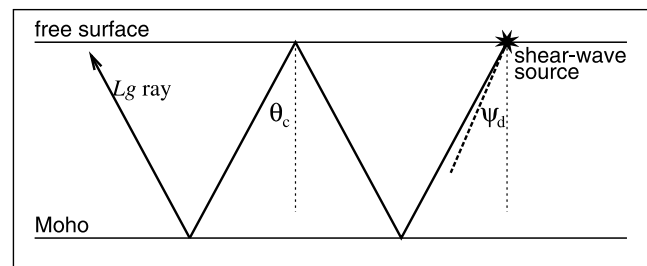


**Figure 20.** Schematic description of *Lg* excitation from *S\**. *Lg* waves originate from the shear energy radiated at post-critical angles. *Lg* can develop from *S\** when the critical reflection angle of shear waves on the Moho is greater than  $\psi_d$ .

[62] **Acknowledgments.** We are grateful to the Incorporated Research Institutions for Seismology for making the seismic data available. The article benefited greatly from the fruitful review comments by William Walter, Jiakang Xie, an anonymous reviewer, and the associate editor. We thank Michael Landes for careful reading the manuscript. This work was supported by the Korea Meteorological Administration Research and Development Program under grant CATER 2007-5111.

## References

- Adushkin, V. V., V. A. An, V. M. Ovchinnikov, and D. N. Krasnoshechekov (1997), A jump of the density on the outer-inner core boundary from the observations of PKiKP waves on the distance about 6 degrees, *Doklady Akademii Nauk*, 354(3), 382–385.
- Aki, K., and P. G. Richards (2002), *Quantitative Seismology*, 2nd ed., University Science Books, Sausalito, CA.
- Aki, K., and Y. Tsai (1972), The mechanism of Love wave excitation by explosive sources, *J. Geophys. Res.*, 77(8), 1452–1475.
- Archambeau, C. B. (1972), The theory of stress wave radiation from explosions in prestressed media, *Geophys. J.*, 29, 329–366.
- Baumgardt, D. R. (1990), Investigation of teleseismic Lg blockage and scattering using regional arrays, *Bull. Seismol. Soc. Am.*, 80, 2261–2281.
- Bonner, J. L., D. C. Pearson, W. S. Phillips, and S. R. Taylor (2001), Shallow velocity structure at the Shagan River test site in Kazakhstan, *Pure Appl. Geophys.*, 158, 2017–2039.
- Brune, J. N., and P. W. Pomeroy (1963), Surface wave radiation patterns for underground nuclear explosions and small-magnitude earthquakes, *J. Geophys. Res.*, 68, 5005–5028.
- Burger, R. W., T. Lay, T. C. Wallace, and L. J. Burdick (1986), Evidence of tectonic release in long-period S waves from underground nuclear explosions at the Novaya Zemlya test sites, *Bull. Seismol. Soc. Am.*, 76, 733–755.
- Day, S. M., and K. L. McLaughlin (1991), Seismic source representations for spall, *Bull. Seismol. Soc. Am.*, 81(1), 191–201.
- Day, S. M., J. T. Cherry, N. Rimer, and J. L. Stevens (1987), Nonlinear model of tectonic release from underground explosions, *Bull. Seismol. Soc. Am.*, 77, 996–1016.
- Eisler, J. D., and F. Chilton (1964), Spalling of the earth's surface by underground nuclear explosion, *J. Geophys. Res.*, 69(24), 5285–5293.
- Ekström, G., and P. G. Richards (1994), Empirical measurements of tectonic moment release in nuclear explosions from teleseismic surface waves and body waves, *Geophys. J. Int.*, 117, 120–140.
- Fisk, M. D. (2006), Source spectral modeling of regional P/S discriminants at nuclear test sites in China and the former Soviet Union, *Bull. Seismol. Soc. Am.*, 96(6), 2348–2367.
- Gupta, I. N., W. W. Chan, and R. A. Wagner (1992), A comparison of regional phases from underground nuclear explosions at east Kazakh and Nevada test sites, *Bull. Seismol. Soc. Am.*, 82, 352–382.
- Gutowski, P. R., F. Hron, D. E. Wagner, and S. Treitel (1984), S\*, *Bull. Seismol. Soc. Am.*, 74(1), 61–78.
- Harkrider, D. G., J. L. Stevens, and C. B. Archambeau (1994), Theoretical Rayleigh and Love waves from an explosion in prestressed source regions, *Bull. Seismol. Soc. Am.*, 84, 1410–1442.
- Helle, H. B., and E. Rygg (1984), Determination of tectonic release from surface waves generated by nuclear explosions in eastern Kazakhstan, *Bull. Seismol. Soc. Am.*, 74, 1883–1898.
- Hong, T.-K., and W. Menke (2008), Constituent energy of regional seismic coda, *Bull. Seismol. Soc. Am.*, 98(1), 454–462.
- Hong, T.-K., and J. Rhie (2009), Regional source scaling of the 9 October 2006 underground nuclear explosion in North Korea, *Bull. Seismol. Soc. Am.*, 99(4), 2523–2540.
- Hong, T.-K., and J. Xie (2005), Phase composition of regional waves from underground nuclear explosion, *J. Geophys. Res.*, 110, B12302, doi:10.1029/2005JB003753.
- Hong, T.-K., R.-S. Wu, and B. L. N. Kennett (2005), Stochastic features of scattering, *Phys. Earth Planet. Inter.*, 148(2–4), 131–148.
- Hong, T.-K., C.-E. Baag, H. Choi, and D.-H. Sheen (2008), Regional seismic observations of the October 9, 2006 underground nuclear explosion in North Korea and the influence of crustal structure on regional phases, *J. Geophys. Res.*, 113, B03305, doi:10.1029/2007JB004950.
- Jepsen, D. C., and B. L. N. Kennett (1990), Three-component analysis of regional seismograms, *Bull. Seismol. Soc. Am.*, 80, 2032–2052.
- Jurkevics, A. (1988), Polarization analysis of three-component array data, *Bull. Seismol. Soc. Am.*, 78, 1725–1743.
- Kennett, B. L. N. (2001), *The Seismic Wavefield*, vol. 1, *Introduction and Theoretical Development*, Cambridge University Press, New York.
- Kennett, B. L. N., E. R. Engdahl, and R. Buland (1995), Constraints on seismic velocities in the Earth from travel times, *Geophys. J. Int.*, 122, 108–124.
- Kim, W.-Y., P. G. Richards, V. Adushkin, and V. Ovtchinnikov (2001), Borovoye digital seismogram archive for underground nuclear tests during 1966–1996, technical report, Lamont-Doherty Earth Observatory of Columbia University, New York.
- Levashova, N. M., K. E. Degtyarev, M. L. Bazhenov, A. Q. Collins, and R. van der Voo (2003), Permian palaeomagnetism of East Kazakhstan and the amalgamation of Eurasia, *Geophys. J. Int.*, 152, 677–687.
- Levshin, A. L., and M. H. Ritzwoller (1995), Characteristics of surface wave generated by events on and near the Chinese nuclear test site, *Geophys. J. Int.*, 123, 131–148.
- Massé, R. P. (1981), Review of seismic source models for underground nuclear explosions, *Bull. Seismol. Soc. Am.*, 71, 1249–1268.
- McLaughlin, K. L., J. L. Bonner, and T. Barker (2004), Seismic source mechanisms for quarry blasts: modelling observed Rayleigh and Love wave radiation patterns from a Texas quarry, *Geophys. J. Int.*, 156, 79–93.
- Myers, S. C., W. R. Walter, K. Mayeda, and L. Glenn (1999), Observations in support of Rg scattering as a source for explosion S waves: Regional and local recordings of the 1997 Kazakhstan depth of burial experiment, *Bull. Seismol. Soc. Am.*, 89, 544–549.
- Nuttli, O. W. (1969), Travel times and amplitudes of S waves from nuclear explosions in Nevada, *Bull. Seismol. Soc. Am.*, 59, 385–398.
- Patton, H. J. (1991), Seismic moment estimation and the scaling of the long-period explosion source spectrum, in *Explosion Source Phenomenology*, edited by S. R. Taylor, H. J. Patton, and P. G. Richards, pp. 171–183, *Geophysical Monograph 65*, American Geophysical Union, Washington, D. C.
- Patton, H. J. (1995), Analysis of Lg spectral ratios from NTS explosions: Implications for the source mechanisms of spall and the generation of Lg waves, *Bull. Seismol. Soc. Am.*, 85, 220–236.
- Ringdal, F., E. Kremenetskaya, and V. Asming (2002), Observed characteristics of regional seismic phases and implications for P/S discrimination in the European Arctic, *Pure Appl. Geophys.*, 159, 701–719.
- Springer, D. L., G. A. Pawloski, J. L. Ricca, R. F. Rohrer, and D. K. Smith (2002), Seismic source summary for all U.S. below-surface nuclear explosions, *Bull. Seismol. Soc. Am.*, 92(5), 1806–1840.
- Stump, B. W. (1985), Constraints on explosive sources with spall from near-source waveforms, *Bull. Seismol. Soc. Am.*, 75, 361–377.
- Taylor, S. (1996), Analysis of high-frequency Pg/Lg ratios from NTS explosions and Western U.S. earthquakes, *Bull. Seismol. Soc. Am.*, 86, 1042–1053.
- Thurber, C., C. Trabant, F. Haslinger, and R. Hartog (2001), Nuclear explosion locations at the Balapan, Kazakhstan, nuclear test site: the effects of high-precision arrival times and three-dimensional structure, *Phys. Earth Planet. Inter.*, 123, 283–301.
- Toksöz, M. N., and H. H. Kehler (1972), Tectonic strain release by underground nuclear explosions and its effect on seismic discrimination, *Geophys. J. R. Astron. Soc.*, 31, 141–161.
- Toksöz, M. N., K. C. Thomson, and T. J. Ahrens (1971), Generation of seismic waves by explosions in prestressed media, *Bull. Seismol. Soc. Am.*, 61, 1589–1623.
- Trabant, C., C. Thurber, and W. Leith (2002), Ground truth seismic events and location capability at Degelen mountain, Kazakhstan, *Phys. Earth Planet. Inter.*, 131, 155–171.
- Vidale, J. E. (1986), Complex polarization analysis of particle motion, *Bull. Seismol. Soc. Am.*, 76(5), 1393–1405.
- Vogfjörd, K. S. (1997), Effects of explosion depth and Earth structure on the excitation of Lg waves: S\* revisited, *Bull. Seismol. Soc. Am.*, 87(5), 1100–1114.
- Wallace, T. C., D. V. Helmberger, and G. R. Engen (1985), Evidence of tectonic release from underground nuclear explosions in long-period S waves, *Bull. Seismol. Soc. Am.*, 75(1), 157–174.
- Walter, W. R., and H. J. Patton (1990), Tectonic release from the Soviet joint verification experiment, *Geophys. Res. Lett.*, 17(10), 1517–1520.
- Walter, W. R., K. Mayeda, and H. J. Patton (1995), Phase and spectral ratio discrimination between NTS earthquakes and explosions, Part 1: Empirical observations, *Bull. Seismol. Soc. Am.*, 85, 1050–1067.
- Walter, W. R., E. Matzel, M. E. Pasyanos, D. B. Harris, R. Gok, and S. R. Ford (2007), Empirical observations of earthquake-explosion discrimination using P/S ratios and implications for the sources of explosion S waves, in *29th Monitoring Research Review: Ground-Based Nuclear Explosion Monitoring Technologies*, pp. 684–693, LA-UR-07-5613.
- Xie, J. (2002), Source scaling of Pn and Lg spectra and their ratios from explosions in central Asia: Implications for the identification of small seismic events at regional distances, *J. Geophys. Res.*, 107(B7), 2128, doi:10.1029/2001JB000509.

T.-K. Hong, Department of Earth System Sciences, Yonsei University, Shinchon-dong, 134, Seodaemun-gu, Seoul 120-749, South Korea. (tkhong@yonsei.ac.kr)